• U C •

FCTUC FACULDADE DE CIÊNCIAS
E TECNOLOGIA
UNIVERSIDADE DE COIMBRA

DEPARTAMENTO DE
ENGENHARIA MECÂNICA

Study on Weldability of Similar Aluminium Alloys by Friction Spot Welding

Submitted in Partial Fulfilment of the Requirements for the Degree of Master in Mechanical Engineering in the speciality of Production and Project

Author

António José Faria de Oliveira

Advisors

Altino J. R. Loureiro

Jorge F. dos Santos

Jury

President	**Professor Doutor Fernando Jorge Ventura Antunes** **Professor Auxiliar da Universidade de Coimbra**
Vowel	**Professor Doutor Rui Manuel Ferreira Leal** **Professor Adjunto Instituto Politécnico de Leiria**
Advisor	**Professor Doutor Altino Jesus Roque Loureiro** **Professor Associado da Universidade de Coimbra**

Institutional Collaboration

Helmholtz-Zentrum Geesthacht
Centre for Materials and Coastal Research

HELMHOLTZ-ZENTRUM GEESTHACHT GMBH
CENTER FOR MATERIALS AND COASTAL RESEARCH
SOLID-STATE JOINING PROCESSES (WMP)

Coimbra, February of 2016

“Live as if you were to die tomorrow. Learn as if you were to live forever.”

Mahatma Gandhi

Aos meus pais.

ACKNOWLEDGEMENTS

It is with deep satisfaction that I express my gratitude to all people that were somehow involved in this work and in my personal progress.

To my professor and advisor Altino Loureiro, for the trust, for opening the door to a great experience and for the words of wisdom during these 6 months;

To Jorge dos Santos, for accepting me at HZG, sharing the knowledge and making an effort along with all his team to make sure my stay would be the best possible;

To Uceu Suhuddin, for the patience and the guidance in everything from the day-to-day activities to the overall direction of the project;

To my colleagues at Geesthacht, "A Malta", for the (really) good times;

To friends in Coimbra, for 5 years I will never forget;

To my friends everywhere else, for making me smile;

To my parents, for putting my education first and for the continuing support and love;

To my brother, because we are a team;

To the rest of my family, for being supportive and proud of our achievements;

To my girlfriend, for being everything I need and so much more, for being my guiding light during this time, far away but ever so bright.

ABSTRACT

The objective of the present work is to access the weldability of a similar configuration of AA5454-H22 by Friction Spot Welding, test the strength of the weld in different configurations and analyse the parameters that contribute to the behaviour of the joint under different types of loading.

The welds were produced in Lap-Shear and Cross-Tensile configuration for static loading experiments and Fatigue samples were also produced to characterize the performance under cyclic loading. Regarding the structural changes introduced by the process, the microstructure was thoroughly examined, the hardness and grain size of each zone were measured and finally the fracture surfaces were observed. The thermal cycle was studied to quantify the variation of temperature with time in the plates.

The weldability study and the use of a Box-Behnken Design of Experiments led to an optimum parameter and the statistical analysis allowed the conclusion that Plunge Depth is the most prominent parameter in the process for this particular material. The most effective welds of the initial range are, generally, the combinations with slower Feeding Rate, higher Rotational Speed and a Plunging Depth of about 20% in the lower plate. Those combinations translate into a high heat input.

Defects such as hook, inadequate bonding and insufficient refill were found in different parameters. The morphology of the hook such as the Bending Angle and the Hook Height proved to have a definite effect on the strength of the welds and on the fracture mode, respectively. According to the data gathered in fracture analysis, the bonding of the plates is stronger in the area directly affected by the sleeve and then gradually decreases towards the centre of the weld, where the bonding is considerably weaker.

Keywords Friction Spot Welding, Solid State Welding, Solid State Joining, Aluminium Alloys, Helmholtz-Zentrum Geesthacht

RESUMO

O objetivo do presente trabalho é o estudo de soldabilidade de uma liga de alumínio AA5454-H22 pelo processo de *Friction Spot Welding* bem como o teste desta soldadura em várias configurações diferentes e a análise dos parâmetros que contribuem para o comportamento da junta sob diferentes carregamentos.

O material foi soldado nas configurações *Lap-Shear* e *Cross-Tensile* de modo a permitir o teste a cargas estáticas. Foram também produzidas amostras para fadiga de modo a caracterizar o comportamento destas quando submetidas a carga cíclicas. Relativamente às mudanças provocadas pelo processo de soldadura, a microestrutura da ligação foi amplamente estudada, foram medidos perfis de dureza e tamanhos de grão em várias zonas e finalmente foram estudadas várias superfícies de fratura. O ciclo térmico foi medido de modo a tentar quantificar o calor transferido para as placas a soldar.

O estudo de soldabilidade e a aplicação de uma técnica de *Design of Experiments*, mais especificamente a técnica *Box-Behnken Design*, permitiu a otimização do processo e a sua análise estatística permitiu concluir que a profundidade de penetração representa o parâmetro que mais contribui para a resistência da soldadura. As soldaduras mais eficazes são, de forma geral, as combinações de parâmetros com menor velocidade de penetração, maior velocidade de rotação e uma profundidade de penetração de cerca de 20% na chapa interior. Estas combinações produzem alta temperatura nos elementos soldados.

Defeitos como o *hook*, *inadequate bonding* e *insufficient refill* podem ser encontrados em diferentes combinações de parâmetros. Aspetos da morfologia do *hook*, tais como o *bending angle* e a *hook height*, provaram ter um efeito determinante na resistência da soldadura e nos modos de fratura, respetivamente. De acordo com a análise de fratura, a ligação entre chapas é mais forte na zona afetada pelo *sleeve*, e gradualmente menor em direção ao centro.

Palavras-chave: Friction Spot Welding, Soldadura no estado sólido, Processos de Ligação no Estado Sólido, Ligas de Alumínio, Helmholtz-Zentrum Geesthacht

CONTENTS

LIST OF FIGURES

LIST OF TABLES

SIMBOLOGY AND ACRONYMS

Simbology

N_R – Number of cycles

σ_a – Alternate stress

σ_m – Mean stress

σ_{max} – Maximum tensile stress

$\Delta\sigma$ – Stress variation

R – Stress ratio

r – Correlation value in Pearson's Product-Moment correlation

α – Bending angle for the hook

μ – Average number of cycles

σ – Standard deviation

h/t – Hook height ratio

Acronyms

ASTM – American Society for Testing and Materials

BB – Box-Behnken

BM – Base material

CF – Clamping force

CR – Clamping ring

CTS – Cross-tensile strength

CTT – Cross-Tensile Testing

DI – Distance between visible interfaces

DoE – Design of Experiments

DT – Dwell time

EDS – Energy Dispersion Spectroscopy

FR – Feeding rate

FSpW – Friction Spot Welding

FSSW – Friction Stir Spot Welding

GKKS – Research Centre Geesthacht

HAZ – Heat affected zone

HH – Hook height

HL – Hook length

HS – Hook slope

HZG – Helmholtz-Zentrum Geesthacht

LSS – Lap-shear strength

LST – Lap-Shear Testing

LSW – Laser Spot Welding

OFAT – One Factor At the Time

OM – Optical microscope

PD – Plunge depth

PP– Pin Plunge

PR – Plunging rate

PT – Plunging time

RFSSW – Refill Friction Stir Spot Welding

RS – Rotational speed

RSW – Resistance Spot Welding

RT – Retracting time

SCC – Stress Corrosion Cracking

SEM – Scanning Electron Microscope

SP – Sleeve Plunge

SPP – Sleeve and Pin Plunge

SZ – Stirred zone

TMAZ – Thermomechanically affected zone

TT – Total time

TWI – The Welding Institute

1. INTRODUCTION

Aluminium is largely known for its unique properties in the material universe. Being versatile and lightweight as well as durable and recyclable, this material has made its way into being used in numerous applications in fields such as transportation, construction and technology.

However, aluminium alloys have proven to be difficult materials to weld due to characteristics like its thermal conductivity and hydrogen solubility. Traditional welding techniques, in most cases, demand large heat inputs and highly skilled labour. That said, new techniques were developed in order to reduce the cost of joining aluminium alloys and also to improve the sustainability of the joining process.

Friction Spot Welding (FSpW), developed at *Helmholtz-Zentrum Geesthacht* (HZG) in Germany, is a solid-state spot joining process that presents an alternative to mechanical and thermal bonding processes such as Clinching, Riveting or Resistance Spot Welding (RSW). Much like Friction Stir Spot Welding (FSSW), FSpW allows the connection between the two parts to be done without the use of filler materials; moreover it has the advantage of doing so without leaving a hole in the end of the process.

Although FSpW has already been tested in some similar and dissimilar combinations of materials with good results, more research is needed in order to better understand the parameters involved and its applications.

The objective of the current work is to test and optimize the welding of similar AA5454-H22/ AA5454-H22 plates with 3 mm of thickness. The thesis is divided in the following stages: State of the Art, where a bibliographic research about the topic is presented; Experimental Procedure, where the methods and the equipment used are described; Results and Discussion, where the data is analysed and finally the Conclusions, where the work and the results are summarized.

2. STATE OF THE ART

2.1. Aluminium Alloys

Even though the aluminium industry is relatively new, this material has grown to be the most produced non-ferrous metal worldwide. Aluminium is the third most abundant element on earth, only surpassed by oxygen and silicon. However, there is no elemental state aluminium in nature, but rather combined forms such as oxides and silicates, and this fact made this element very rare and expensive in its early stages of production.

Aluminium's existence was established in 1808 by an English chemist and physicist, Sir Humphrey Davy. Nevertheless, it took 17 years for the first pellet of material to be produced. This feat was accomplished by the Danish physician Hans Christian Oersted in 1825, at the Royal Danish Academy of Science and Letters. Although many improvements were made ever since in order to reduce the production cost, today's model is based in the electrolytic method devised in 1886 by Paul Louis Touissant Héroult of France and Charles Martin Hall of the United States of America, who worked independently and almost simultaneously came up with the same idea.

The first and second World Wars had a major effect on the production of this metal as its characteristics proved to suit the military needs of the countries involved. Thus, at the end of World War II there was a huge production capacity of aluminium and not much military demand. This led to the development of civilian markets for this material and to the never-ending list of applications seen today. (RUSAL, 2015; Cobden *et al*, 1994)

2.1.1. Wrought Alloys & Temper Designations

The classification of aluminium alloys is based on the predominant alloying elements. The first digit represents the main component besides aluminium and defines the series as shown in Table 2.1; the second digit indicates modifications made to the existing alloy; the third and fourth digits represent the degree of purity in the case of 1xxx series, as for the other series these digits just serve as a way to differentiate between different alloys. (AZOMaterials, 2015; MATTER & University of Liverpool, 2010)

Table 2.1 – Wrought aluminum alloys designation system

Series	*Main Alloying Elements*	*Treatability*
1xxx	Pure Aluminium, > 99% Al	Non-Heat-Treatable
2xxx	Copper (Cu)	Heat-Treatable
3xxx	Manganese (Mn)	Non-Heat-Treatable
4xxx	Silicon (Si)	Non-Heat-Treatable
5xxx	Magnesium (Mg)	Non-Heat-Treatable
6xxx	Magnesium (Mg), Silicon (Si)	Heat-Treatable
7xxx	Zinc (Zn)	Heat-Treatable
8xxx	Other Elements	Not Applicable

Aluminium alloys can be divided in heat-treatable and non-heat-treatable and according to this distinction, different treatments can be applied. The temper designations can be identified as the hyphenated suffix containing a letter, according to Table 2.2, and one or more digits to specify the details of the treatment.

Table 2.2 – Basic temper designations for wrought alloys

Designation	*Description*
F	As fabricated
O	Fully Annealed
H	Strain hardened
T	Heat Treated
W	Solution Heat Treated

2.1.2. 5xxx Aluminium Alloys

5xxx series aluminum alloys are non-heat-treatable and have magnesium as their main alloying element. This group of materials finds a lot of its application when outdoor exposure is needed, due to its excellent corrosion resistance combined with medium strength, good weldability and formability. Thus, marine, automotive and architectural sectors are the main users of this series of alloys. The strength of 5xxx series alloys generally increases along with the magnesium content and has the possibility of being enhanced through cold work. Nonetheless, if the magnesium content is higher than 3.5 %, there is the risk of stress corrosion cracking (SCC) if subjected to higher temperatures than the recommended. (ALCOA Inc., 2015; MATTER & University of Liverpool, 2010)

2.1.3. AA5454-H22

AA5454 can be characterized as a medium-to-high strength alloy with excellent corrosion resistance, high fatigue strength, good weldability and formability. Its anti-corrosion qualities make this alloy very efficient for seawater applications such as offshore structures or ship components. This material is also used in the chemical industry to build pressure vessels, tank and boilers, as well as the in the transportation sector to produce body parts or fuel tanks. Regarding the chemical composition, the increase of the magnesium and chromium content tends to increase the corrosion resistance along with the fatigue strength of this alloy. The H22 treatment corresponds to strain hardening and partial annealing to quarter hard condition. (Engler *et al*, 2013; MATTER & University of Liverpool, 2010; Metal Suppliers Online, 2015; ALCOA Inc., 2015)

2.2. Friction Stir Welding

Friction Stir Welding is a solid-state joining process invented at *The Welding Institute* (TWI) in the United Kingdom and patented in 1991. Initially, this technique was only applied to butt welds in aluminium alloys, but the evolution of the welding technique and tools allowed it to be used in multiple configurations and materials today.

This method consists of plunging a rotating tool, comprised of a shoulder and a pin, into two abutting plates and traversing this non-consumable tool along the line of joint as shown in Figure 2.1.

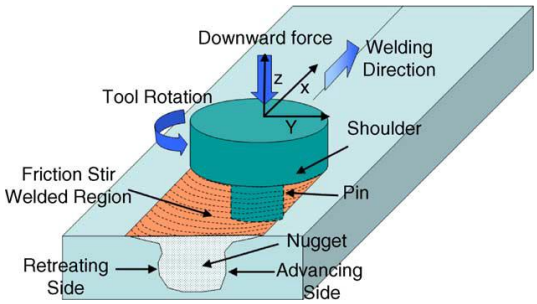

Figure 2.1 – Schematic drawing of FSW (Mishra & Ma, 2005)

The frictional heat generated between the tool and the plates causes the material to plasticize and its traverse movement allows the blending of the material and the formation of the welded nugget (Çam & Mistikoglu, 2014).

According to Mishra & Ma (2005) the most influential parameter in the process is the tool geometry. Besides tool geometry, tool rotation rate, traverse speed and tool tilt are also important variables to take into account when controlling heat input and material flow.

FSW has one of the quickest growths in terms of industrial implementation when compared to other welding processes (Threadgill, 2010). This increasing popularity can be attributed to qualities such as its relatively low cost and energy input as well as the metallurgical advantages of being a solid-state process.

2.3. Other Spot Joining Processes

Friction Stir Spot Welding (FSSW) is a variant of FSW invented by Mazda Motor Corporation in 1993. The tool needed for FSSW is similar to FSW, also having a pin and a shoulder. However, traverse speed is not applied in this method. The process is divided in three stages: plunging, stirring and retracting. The tool rotation rates and the total plunging time will have the ultimate influence on heat input and material flow (Yang *et al*, 2014).

The main disadvantage of both FSW and FSSW is the characteristic keyhole left by the tool at the end the weld. This feature significantly decreases the mechanical properties of the joint.

Some others variants of friction have been recently catalogued by Yang *et al* (2014) such as Pinless FSSW, Swing FSSW and a novel FSSW process. All images concerning these processes are presented in Annex A. The Pinless FSSW process is pictured in Figure A.0.1 and presents a simpler alternative to the standard techniques that produces high strength fast welds with a good appearance. Swing FSSW is variation of the typical FSW where the path of the tool is circular instead of being linear, as shown in Figure A.0.2. Although this technique does not remove the keyhole defect, it increases the welded area and consequently the strength of the welds. The novel FSSW process, pictured in Figure A.0.3, uses a specially designed tool and back plate, containing a round dent, to where the material flows during the weld. In the second step of the process, a flat back plate is employed to the keyhole of the top plate and to the protuberance of the back plate. This process has been successfully applied to AA6061 and AA5052.

2.4. Friction Spot Welding

Friction Spot Welding (FSpW), also known as Refill Friction Stir Spot Welding (RFSSW), was developed by the *Helmholtz-Zentrum Geesthacht* (HZG), formerly known as GKSS, in 2002. This method is used exclusively to make spot welds and is nowadays a viable option in a great amount of applications and materials, either in similar or dissimilar joints. The tool assembly is comprised of three distinct parts as shown in Figure 2.2: pin, sleeve and clamping ring.

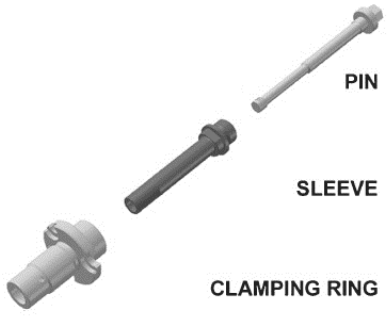

Figure 2.2 – Example of FSpW tools (adapted from Amancio-Filho *et al*, 2011)

Both pin and sleeve are rotating parts connected to one motor for rotational speed, but independently actuated in terms of axial displacement. The clamping ring (CR) is stationary and its axial displacement is managed by a third actuator that moves the entire welding head towards the plates (Rosendo *et al*, 2011). This component has the purpose of keeping the plates-to-be-welded tightly secured and also avoiding the loss of material during the process. The pin and the sleeve, on the other hand, are used to plunge into the plates and mix the materials.

There are several advantages in the application of this technology. FSpW allows the welding of a large array of materials such as aluminium, steel, magnesium and thermoplastics, either in similar or dissimilar configuration. In comparison with Mechanical Fastening, FSpW suppresses the weight penalty, the difficulty of automation and, being watertight, the requirement of sealants and the corrosion problems. Regarding Fusion Spot Welding processes like Laser Spot Welding (LSW) and Resistance Spot Welding (RSW), FSpW represents a huge decrease in the energy input and therefore a better preservation of the properties of the base material (Amancio-Filho *et al*, 2011).

Even though Friction Stir Spot Welding is a solid-state process and presents a good alternative to previously used methods, this technique has some drawbacks. The mandatory key-hole defect left in the weld and subsequent decrease of the effective cross section turn out to affect greatly the performance of the joint. For these reasons FSpW presents a viable option for lap or butt welding of thin sheets of several materials. Nonetheless there are different variants with which FSpW welds can be done: Sleeve Plunge; Pin Plunge and Sleeve & Pin Plunge.

2.4.1. Sleeve Plunge

According to Rosendo *et al* (2011) the Sleeve Plunge (SP) method can be divided into four stages, as shown in Figure 2.3.

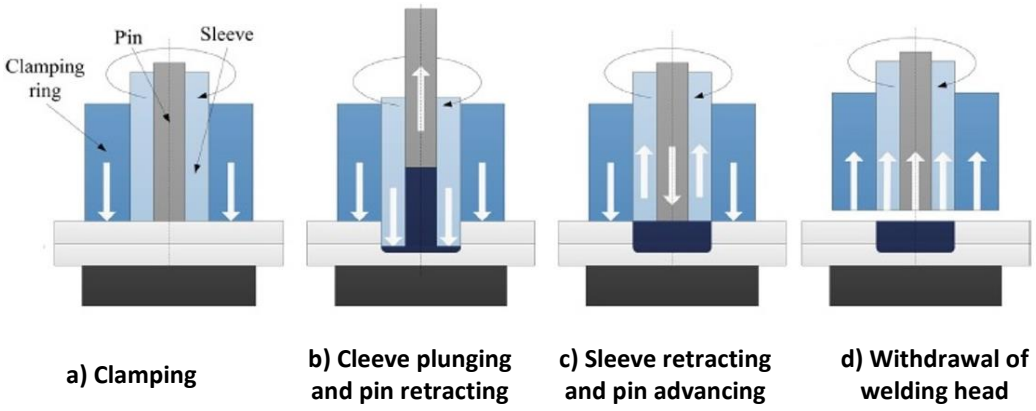

Figure 2.3 – Representation of Sleeve Plunge FSpW process (Zhao *et al,* 2014)

On the first stage, the plates are clamped against the anvil by the clamping ring while the pin and the sleeve start rotating and produce frictional heat on the surface of the upper sheet. The second stage consists on the plunging of the rotating sleeve through the plates whereas the pin is retracted. The upward movement of the pin creates space to accommodate the material displaced by the penetration of the sleeve. After stage two, both pin and sleeve are brought back to the clamping position: the sleeve is retracted from the plates and the pin advances until the initial position, pushing back the material towards the plates. The second and third stages allow the weld to be done without the keyhole defect seen in FSSW. The final stage is the withdrawal of the welding head. The area directly affected by the pin and the sleeve is commonly called the welding nugget.

The Sleeve Plunge method offers a wide bonding area between the two plates and generally a stronger weld. Consequently, this technique is the most used in the existing literature.

2.4.2. Pin Plunge

The Pin Plunge method (PP) is very similar to the Sleeve Plunge variant. These two processes actually share the first and the fourth stages presented earlier. Thus, after the plates are properly clamped and the pin and the sleeve are already rotating, the pin is plunged through the plates and the sleeve is retracted. The material displaced by the pin is accommodated between the pin and the shoulder due to the axial displacement of the sleeve. Finally, pin and sleeve are moved back to the clamping position and the welding tool is withdrawn from the plates.

This technique has the advantage of demanding less torque from the welding apparatus as a result of having a smaller plunging element. However, the bonding area is significantly smaller than in the Sleeve Plunge method, leading to a decrease in the strength of the weld and consequently in the application of Pin Plunge method (Amancio-Filho *et al*, 2011).

2.4.3. Sleeve & Pin Plunge

The Sleeve & Pin Plunge method (SPP) essentially joins the two previous methods while using the same tool. The process also starts with the clamping of the plates by the stationary clamping ring. Afterwards, the sleeve is plunged into the plates while the pin retracts. Unlike the Sleeve Plunge method, instead of returning to the clamping position, the pin is plunged in the material and the sleeve is retracted as seen in the Pin Plunge method. Finally, all the parts move back to the clamping position and the welding head is withdrawn from the plates.

This technique was used by Venâncio (2013) in order to improve the welding characteristics of a 1 mm thick AA6082-T6 aluminium alloy. A significant improvement in the properties was observed, although no further studies have been done concerning the viability of this method. The obvious increase of effective welding time in comparison to the previous methods presents an important drawback to the implementation of this technique.

2.5. Welding Parameters

The correct choice of parameters is of extreme relevance when projecting a weld by FSpW. These parameters can change drastically depending on the material, the application and the working conditions of the weld. For instance, some applications might need a particularly strong weld whereas other might only need a fast weld. Some applications might require a good behaviour in a specific type of loading condition or in various types. For this reasons it is very important to study previous works in order to adapt the parameters to the application and base material. Table 2.3 is a compilation of the various parameters found in the existing literature.

Table 2.3 – Summary of the parameters collected in the literature review

Authors	*Material Combination*	*Thickness [mm]*	*Rotational Speed [rpm]*	*Total Time [s]*	*Feeding Rate [mm/s]*	*Plunge Depth [mm]*	*Clamping Force [kN]*	*Observations*
(Rosendo et al, 2011)	AA6181-T6/ AA6181-T6	1.7	1900; 2400; 2900	2,0; 2,2; 2,6; 3,0; 3,4	-	1.75	non-specified	Sleeve Plunge
(Tier et al, 2013)	AA5042/ AA5042	1.5	900; 1400; 1900	-	[0,47; 1,87]	1.45; 1.55	non-specified	Sleeve Plunge
(Shen et al, 2014)	AA6061-T4/ AA6061-T4	2	1500; 1800; 2100	2; 3; 4	-	2.2	18	Sleeve Plunge
(Amancio-Filho et al, 2011)	AA2024/ AA2024	2	1900; 2400; 2900	4.8; 5.8; 6.8	-	2.5	non-specified	Sleeve Plunge; Pre-heated tools 150ºC
(Suhuddin et al, 2014)	AA5754/ AZ31	1	1500; 1900; 2300	[4; 6] (TT); [0;2] (DT)	-	1.4; 1.6; 1.8	12	Sleeve Plunge
(Campanelli et al, 2013)	AZ31/ AZ31	2	1000; 1500; 2000	[4; 6] (TT); [0;2] (DT)	-	2.25; 2.50; 2.75; 3.00	non-specified	Sleeve Plunge
(Suhuddin et al, 2013)	AA5754/ AZ31	1	1900	2 (DT)	0,8	1.6	12	Sleeve Plunge
(Venâncio, 2013)	AA6082-T6/ AA6082-T6	1	1900; 2000; 2200	non-specified	non-specified	0.6, 1;1.4 (pin) 1; 1.3; 1.6 (sleeve)	10	Sleeve & Pin Plunge
(Shen et al, 2013)	AA7075-T6/ AA7075-T6	2	1500; 1750; 2000	3; 4; 5	-	non-specified	non-specified	Sleeve Plunge
(Zhao et al, 2014)	7B04-T74/ 7B04-T74	1.9	1500	4; 5; 6; 7	-	2; 2.5; 3; 3.5	non-specified	Sleeve Plunge

Rotational speed (RS) has a big influence on the heat input. The faster the pin and the sleeve are rotating, the more frictional heat will be produced. Consequently, the plasticity of the material will increase and allow, to a certain extent, a better blending of the materials. The lack of fluidity caused by insufficient rotational speeds can prevent the material that is displaced by the sleeve to fill the gap left by the pin. On the other hand, excessive rotational speeds can also have a negative effect on the weld. Too much temperature will degrade the properties of the material and it has been observed that high rotational speed can promote slippage between the plates and the tool, affecting the material flow (Rosendo *et al*. 2011). This is also known as the Slip/Stick Transition Phenomena (Campanelli *et al*, 2013).

Total time (TT) is the sum of the plunging time (PT), the retracting time (RT) and the dwell time (DT). Plunging time and retracting time correspond to the second and third stages of the FSpW process, respectively. Dwell time is a time interval that can be applied between stages in order to increase the heat input. Together with rotational speed, total time has a major influence on the heat input. Total time has to be enough to guarantee material plastization however, if the process takes too long, there is the risk of reaching temperatures where the properties start degrading.

Some authors measure the plunging rate (PR) or feeding rate (FR) instead of total time, nevertheless the rate and time are easily convertible through the plunging depth.

Plunging depth (PD) represents the axial displacement that the plunging element undergoes, starting at the clamping position. This value varies from just under 50% of the combined thickness of the plates up to 90%. If the value of plunge depth is too low, there is the risk of jeopardizing the bond between plates, however the increase of plunge depth can also represent a greater deformation on the plates and a larger heat input.The displacement of the retracting element, such as the pin in Sleeve Plunging, is calculated based on the volume displaced by the plunging element in order to accommodate the same amount of material.

Clamping force (CF) is the vertical force applied by the clamping ring in the plates. The value of this parameter has to be enough to secure the plates and prevent the loss of material. Nevertheless, if this value is excessive regarding the thickness of the plates, there is an inherent risk of deformation which can be harmful to the process.

The effects of each parameter are intrinsically related. Thus, many authors have concluded that a sound connection does not result from a correct value of a single parameter but rather the correct parameter combination.

2.6. Microstructure and Hardness profiles

Although Solid State Processes have a relatively low energy input, the base material is submitted to a great amount of microstructural changes. The affected area is commonly divided in three zones as pictured in Figure 2.4: stirred zone (SZ); thermomechanical affected zone (TMAZ); and heat affected zone (HAZ).

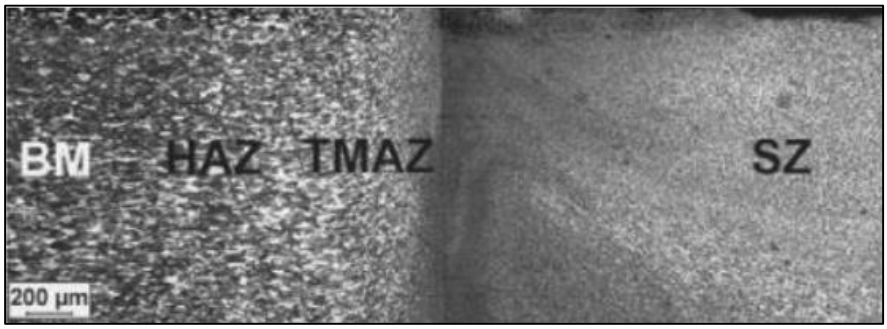

Figure 2.4 – Zone division after welding (Amancio-Filho *et al,* 2011)

The stirred zone is directly affected by the pin and the sleeve. As a result, the material is subjected to high strain rates and thermal cycles that cause the grains to recrystallize and consequently become very refined and equiaxed. The termomechanically affected zone is characterized by highly deformed and elongated grains originated by the tool motion. The heat affected zone is sometimes not easily distinguished from the base material yet some materials show slight transformations in this area worth noticing (Rosendo *et al*, 2011; Campanelli *et al*, 2013)

The hardness profiles across the welds depend not only on the welding parameters but also on the temper of the material prior to welding. In the case of aluminium alloys there are two main groups: heat-treatable al-alloys and non-heat-treatable al-alloys. This division determines what treatments can be applied to each material and therefore it has great influence on the way the material will react to the welding process (Çam & Mistikoglu, 2014).

Etter *et al* (2007) analysed the microstructure of the non-heat treatable AA5251-H14 and AA5251-O alloys welded by FSW to better understand the temper's influence on

the final result, and emphasized the different recrystallization mechanisms occurring in each workpiece. In the case of the annealed alloy, AA5251-O, there are no significant differences regarding the transition from BM to HAZ, whether in terms of microstructure or hardness. In the TMAZ, however, the grain becomes elongated and misoriented, suggesting the occurrence of geometric dynamic recrystallization. The SZ presents recrystallized fine and equiaxed grains. Figure 2.5 shows the effect of FSW in the hardness for different tempers.

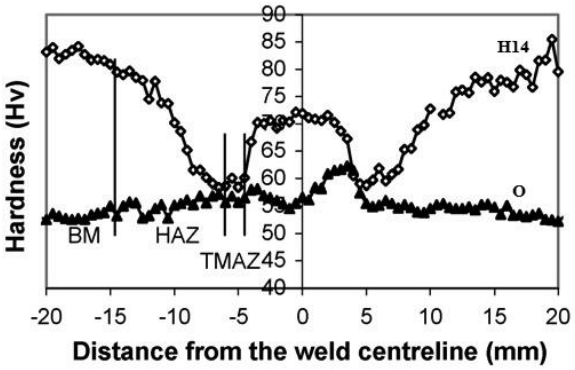

Figure 2.5 – Hardness profiles of both AA5251-H14 and AA5251-O (Etter *et al,* 2007)

The strain hardened specimen, AA5251-H14, shows a considerably higher initial value of hardness compared to the annealed alloy. The HAZ in this specimen, in contrast with the annealed specimen, displays a drastic reduction of the hardness value, explained by the static recrystallization occurring in this area that replaces the initial elongated grain structure. The hardness in the TMAZ is the lowest of the entire affected zone after experiencing dynamic recrystallization. In the SZ, on the other hand, the hardness values increase again due to its fine, equiaxed recrystallized grain.

Shen *et al* (2014) studied the microstructure and mechanical properties of the heat-treatable AA6061-T4 after FSpW and registered the same three distinct zones previously referred. The HAZ displayed a slight decrease in hardness possibly due to grain coarsening. The hardness loss in the TMAZ is much more pronounced and this variance is attributed to the dissolution of precipitates caused by the higher thermal cycle. The grains in this zone are highly deformed. In the area affected directly by the tool the hardness rises and is relatively uniform in the nugget. This occurrence is credited to the violent stirring suffered by the plates or some reprecipitation in this area. The hardness profiles of these welds exhibit what is usually called “w-shaped appearance”.

2.7. Weld Defects

Although FSpW does not promote typical fusion welding defects, such as porosity or solidification cracking, the characteristics of this solid state process also generate certain flaws that can affect the strength of the joint. If defects such as hook, voids, annular groove, inadequate bonding and insufficient refill take large enough proportions, the mechanical strength of the weld can be compromised.

The hook is a very common defect in FSpW, characterized by a path deviation of the interface of the plates, as pictured in Figure 2.6.

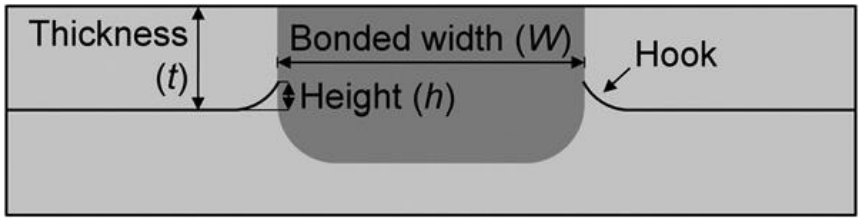

Figure 2.6 – Representation of the hook defect (Campanelli *et al,* 2013)

Badarinarayan *et al* (2009) observed an upward bending of the interface and attributed the formation of this irregularity to the tool penetration on the bottom sheet. Shen *et al* (2013), on the other hand, detected an L-shaped downward hook with poor continuity and credited this to poor mixing and tool penetration on the bottom sheet. The hook, although in different shapes, is found on the majority of the welds and acts as crack nucleation site. Therefore the study of these flaws is becoming increasingly important. Rosendo *et al* (2011) identified an upside V-shaped hook and concluded that the sharper the hook got, the easier it is for this defect to become a crack nucleation site. A strong relation between the hook's sharpness and the total time of the weld was also noticed. Campanelli *et al* (2013) measured the *h/t* ratio which, as shown in Figure 2.6, represents a relation between the height of the hook and the original plate thickness. It was concluded that this ratio also had influence on the fracture mode of the weld.

Voids are craters without material that appear in some parts of the welding nugget as pictured in Figure 2.7. The occurrence of these defects has obvious repercussions on the integrity and mechanical properties of the weld, especially when subjected to external load (Shen *et al*, 2013). Shen *et al* (2014) linked these imperfections to insufficient material flow and observed that voids preferably form in the hook area and on the sleeve's path.

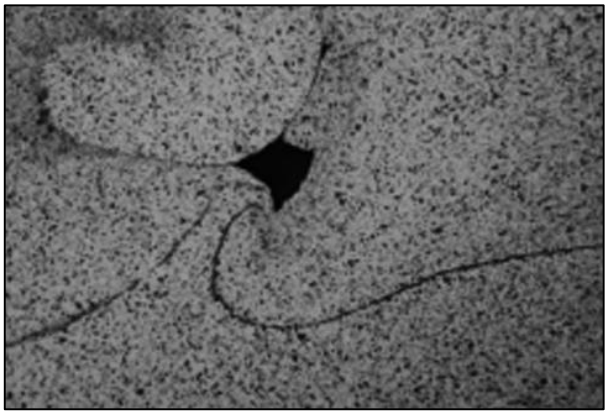

Figure 2.7 – Microscopic Image of the void defect (Shen *et al,* 2014)

The bonding ligament is described by Rosendo *et al* (2011) as a region where the bond between the upper and lower plates is robust. This region exhibits a characteristic banded structure on the centre and an "inclined zigzag" on the edges, caused by the displacement of material from the pin on the third stage of FSpW (Shen *et al*, 2014). Inadequate bonding, on the other hand is described as a region of bad adhesion between the two sheets and is detrimental to the soundness of the weld because its increase directly translates in a smaller bonding ligament (Tier *et al*, 2013).

Incomplete refill is a defect caused mainly by inaccurate selection of the welding parameters. Lack of mixing and insufficient material flow can lead to an improper refill of the original plunging hole during stage three of FSpW. This has obvious consequences on the overall look of the welding nugget and defeats the purpose of FSpW by not achieving a key-hole free nugget (Rosendo *et al*, 2011).

Zhao *et al* (2014) described the annular groove defect as being the consequence of the extrusion of plasticized material into the gap between the clamping ring and the sleeve. As there is no possibility for the material in this gap to be extruded back into the welding nugget, the annular groove creates material shortage. The dimensions of this defect increase with higher sleeve plunge depths as there is more displaced material to be accommodated between the two parts of the tool.

2.8. Lap-Shear Testing

Lap-Shear Testing (LST) determines the shear strength of a welded joint and is used in most of the existing literature about FSpW as the criteria to define the viability of a certain combination of welding parameters.

Tier *et al* (2013) studied the shear strength of similar 1.5 mm thick AA5042 welds and reported that the highest shear loads were clearly associated with lower rotational speeds. It was also stated that plunging rate does not have an important role in the lap shear testing of this configuration, as there were welds processed with the same plunging rate that presented completely different results.

Shen *et al* (2014) performed FSpW in 2 mm thick AA6061-T4 and concluded that the relation between the parameters and the final lap-shear strength (LSS) was not linear. For a total time of 2 seconds, the strength started to rise with the increase of rotational speed but after a certain optimal value started to decrease. For total times between 3 and 4 seconds though, it was established that rotational speed did not have a significant effect on the LSS. Rosendo *et al* (2011) reported a situation with some similarities in 2 mm thick AA6181-T4. Unlike Shen *et al* (2014), for a total time of 2.6 seconds, the increase of rotational speed caused a constant decrease of LSS. However it was noticed that, for the optimum total time, the rotational speed also had little effect on the final LSS.

Zhao *et al* (2014) applied FSpW to 2 mm thick AA7075-T6 and established that the best mechanical properties were obtained with the lowest total times and the lowest rotational speeds. The authors also stated that given a certain high rotational speed, the extension of the duration time would contribute to an improvement of the mechanical properties of the weld.

While studying the mechanical behaviour of friction spot welded 2 mm thick AA2024, Amancio-Filho *et al* (2011) concluded that at a low total time, the increase o rotational speed would increase the shear strength of the specimen. Inversely, at high total times, the increase of rotational speed would lower the LSS. The authors also detailed that at optimum rotational speed, the total time had little interference on the final result.

2.9. Cross-Tensile Testing

Cross-Tensile Testing (CTT) is used to determine the pure tensile strength of a weld without having the side effects of bending experienced in other testing techniques.

Shen *et al* (2013) investigated the microstructure and failure mechanisms of AA7075-T6 friction spot welds and stated that the relation between parameters and cross-tensile strength (CTS) is quite complex. Although the highest strengths were associated with

lower rotational speeds, the connection between rotational speed and total time is not linear. For instance, at low rotational speeds, an increase in strength can be obtained by a reduction of the total time. Yet, with higher rotational speeds, the strength is maximized by the increase of total time. It was also possible to conclude that there was a direct correlation between the size of the voids and the mechanical properties.

Shen *et al* (2014) also stated the complexity of the relation between the parameters and the cross-tensile properties while studying the microstructure and mechanical properties of AA6061-T6 friction spot welds. For low rotational speeds, the strength increased with the increase of rotational speed. However, at higher rotational speeds the strength starts to increase and then decreases when a constant increment of total time is applied. It is also worth noticing that there was no relation found between the geometry of the hook and the mechanical strength of the welds.

2.10. Fatigue Testing

The fatigue failure of a component or material is the process of permanent, progressive and localized structural modification when subjected to dynamic loadings. These loadings can result in cracks or even component failure given a certain number of cycles. This phenomena was first recognized in the early 1800s when European investigators observed the cracking of bridge and railroad components when subjected to repeated loading *(*Branco *et al*, 2012; ASM International, 2008).

Fatigue crack nucleation and propagation is divided in three stages: crack initiation, crack propagation and ultimate failure. Crack initiation usually occurs in a notch or surface discontinuity. In the case of a defect-free surface, persistence slip bands can be formed as a result of the systematic build-up of fine slip movements. The back-and-forth movement of the slip bands can eventually form a crack. Crack propagation occurs when the initial crack starts propagating in a direction normal to the applied stress. Crack propagation can also induce the creation of fatigue striations, each representing a fatigue cycle, as well as the creation of concentric markings on the surface, often called beach marks. Ultimate failure is the moment when the fatigue crack is so deep that the remaining cross section cannot withstand the applied stress.

In order to cause failure by fatigue, it is necessary to fulfill three basic factors: a sufficiently high maximum tensile stress (σ_{max}); a large enough variation of the applied stresses ($\Delta\sigma$); and a sufficient number of cycles (N_r). Although there is a large number of fluctuation stresses, the types of loading pictured in Figure 2.8 are the most common.

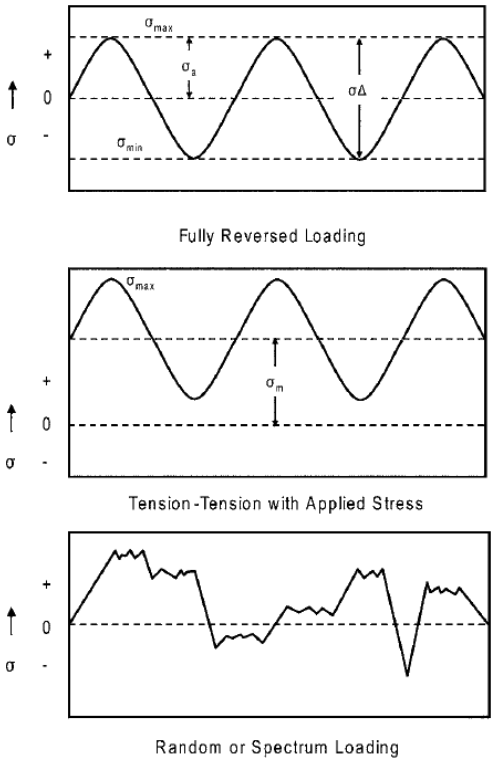

Figure 2.8 – Main types of stress cycles (ASM International, 2008)

Fully reversed loading is characterized by a null mean stress (σ_m), which implies that the maximum and minimum tensile stresses have the symmetrical values and consequently the stress ratio R, which is the quotient of the minimum tensile stress divided by the maximum tensile stress, takes the value of -1.

Tension-tension with applied stress is a kind of cycle defined by a non-negative mean stress. This means that the sample will always be under tension and the R ratio will be positive.

Random or spectrum loading is regarded as a type of cycle where the loading patterns change and normally is the most realistic way to represent the working conditions of a moving part. (ASM International 2008).

Regarding FSpW joints, no publications were found with fatigue studies.

3. EXPERIMENTAL PROCEDURE

3.1. Material and Preparation

3.1.1. AA5454-H22

The chemical composition and mechanical properties of the 5454 aluminium alloy are presented in Table 3.1 and Table 3.2, respectively. The material was delivered in order to accommodate three different configurations, all of which with 3 mm of thickness, in order to perform lap-shear, cross-tensile and fatigue tests. The lap-shear specimens' dimensions are 100 mm x 25 mm x 3 mm, as shown in Figure 3.1, and were assembled to obtain a 25 mm overlap region. The cross-tensile specimens' dimensions are 150 mm x 50 mm x 3 mm and had 20 mm holes drilled on each end of the plate, to allow the execution of the test, as pictured in Figure 3.2. The fatigue test specimens have a similar geometry to the lap-shear samples, as shown in Figure 3.3, with the difference of having 10 mm diameter holes drilled on one end of the plates to ensure compatibility with the fatigue machine.

Table 3.1 – Chemical composition of AA5454-H22 (MATTER & Liverpool, 2010)

Element	*Mg*	*Mn*	*Fe*	*Si*	*Cu*	*Zn*	*Cr*	*Ti*	*Other Elem*	*Total Other*	*Al*
%	2.4-3.0	0.50-1.0	≤0.40	≤0.25	≤0.10	≤0.25	0.05-0.20	≤0.20	≤0.05	≤0.15	Rem.

Table 3.2 – Physical and mechanical properties of AA5454-Hx2 (MATTER & Liverpool, 2010; M. Suppliers Online, 2015)

Elasticity Modulus (GPa)	70.5
Yield Strength (GPa)	245
Tensile Strength (MPa)	265
Elongation (%)	15
Hardness (HV)	60
Poisson Coefficient	0.33
Melting Point (˚C)	607

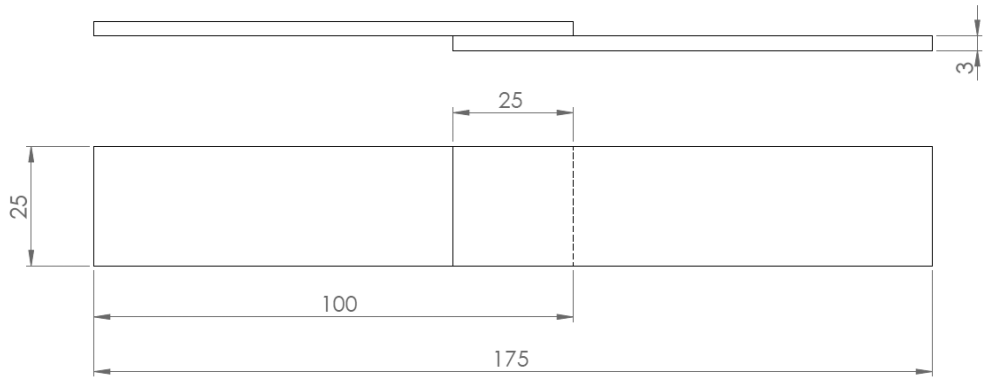

Figure 3.1 – Geometry of the lap-shear specimens

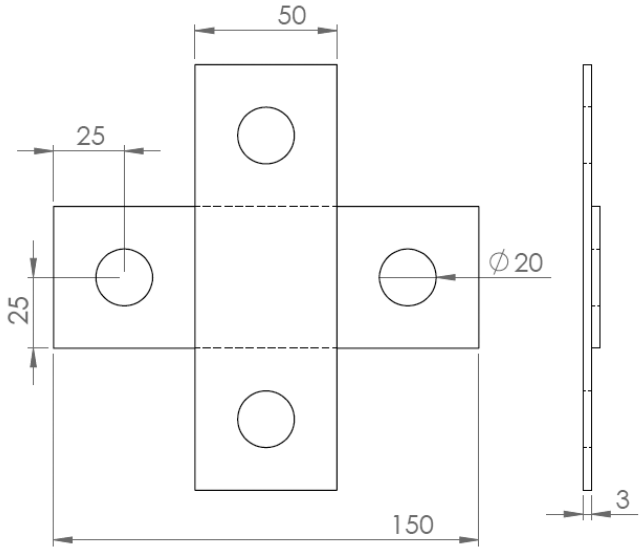

Figure 3.2 – Geometry of the cross-tensile specimens

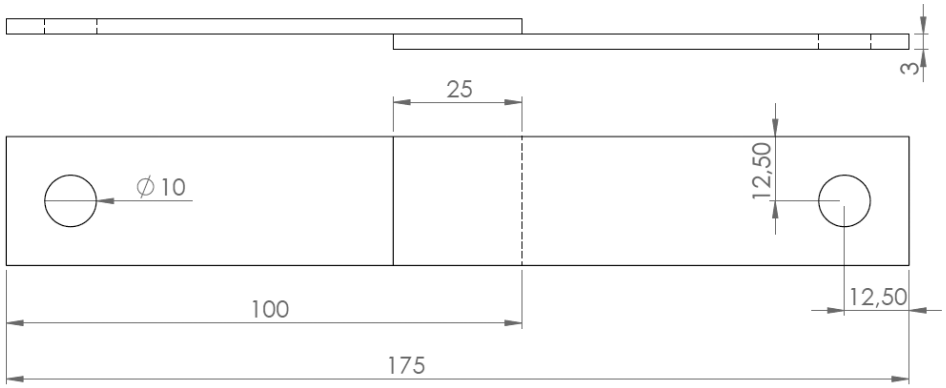

Figure 3.3 – Geometry of the fatigue specimens

3.2. FSpW Equipment

The friction spot welds were executed in *Helmholtz-Zentrum Geesthacht*, by a *Harms & Wende RPS100* machine. The interface software on this equipment allows the programming of the rotational speed of both pin and sleeve, as well as the plunging depth of the tools and the time interval of each stage. This machine's technical features include a maximum clamping force of 20 kN, a maximum rotational speed of 3300 rpm and a maximum torque of 14.5 N·m. Complete details about the equipment can be found on Table 3.3. The dimensions of the tool can be seen in Table 3.4. All welds were performed with the Sleeve Plunge method.

Table 3.3 – Detailed technical information of *Harms &Wende RPS100*

Weight (kg)	65
Stroke of the welding head and table (mm)	12
Stroke of the tools (mm)	10
Welding force (kN)	20
Maximum rotational speed (rpm)	3300
Maximum applicable torque (N·m)	14.5

Table 3.4 - FSpW tool dimensions

Tool Part	Outer diameter
Pin	6 mm
Sleeve	9 mm
Clamping Ring	17 mm

3.3. Design of Experiments

The use of a Design of Experiments (DoE) has the objective of minimizing the total experiments needed to obtain a statistical background to validate a certain combination of parameters. For this reason, a three parameter Response Surface Box-Behnken DoE was chosen and the three selected parameters were rotational speed, plunge depth and feeding rate. The clamping force was fixed at 13.25 kN as this value proved to be enough to perform the weld without creating an excessive indentation of the plates. The response factor in the DoE made for Lap-Shear Testing is the lap-shear strength, meaning that the welds will be judged exclusively on their LSS. In the case of Cross-Tensile Testing, the only response

factor was cross-tensile strength. All DoE related calculations were performed in the *Minitab* software.

So that a proper input to the Design of Experiments is guaranteed, it was necessary to elaborate a weldability study of the feasible combinations of parameters. The initial choice of parameters was also based on previous FSpW studies and articles.

In a later stage of the LST study the One Factor At the Time (OFAT) method was used to evaluate the effect of each parameter individually on the microstructure and strength of the welds. This method consists of setting a base parameter combination and changing one parameter while maintaining the others. In this particular case, the base parameter combination of the OFAT was the optimum parameter combination previously found by the Box-Behnken DoE.

3.4. Mechanical Characterization

Lap-Shear Testing was carried out in a *Zwick-Roell 1478* universal tensile machine, with a nominal load capacity of 100 kN. The experiments were conducted at room temperature, with a free length between clamps of 129 mm and a crosshead speed of 2 mm/s. Although the dimensions of the specimen are not accordant to the norm, the test were performed according to the Resistance Spot Welding standard (ISO International, 2014). The Cross-Tensile Testing was also performed in the same tensile machine, although using a different clamping system to accommodate the geometry of the specimens. The crosshead speed was 2 mm/s. The tests were carried out according to the RSW standard for CTT (ISO International, 2000). Lap-shear and Cross-tensile testing schemes can be seen in Figure 3.4.

Fatigue Testing was executed according to the RSW norm for fatigue testing (ISO International, 2003) in two Shenck Servohydraulic (25 kN of maximum load and 125 mm of maximum displacement) and a Shenck Servohydraulic (10 kN of maximum load and 20 mm of maximum displacement). The data was processed by the *Desilap 7* software. The test frequency was 20 Hz, considering an *R* value of 0.1 and that the fatigue limit is reached when a sample surpassed 5×10^6 cycles.

The hardness tests were performed in a *Zwick&Roell* ZHV linked to the *TestXpert* data acquisition software. The chosen applied load was 300 gf ($HV_{0.3}$) during 10 seconds. The indentations were executed at half thickness of the upper and lower plates, with

0.3 mm between each. The indentation lines started 0.5 mm from the end of the plate and a total of 80 indentations were made in each line so that all weld zones were covered.

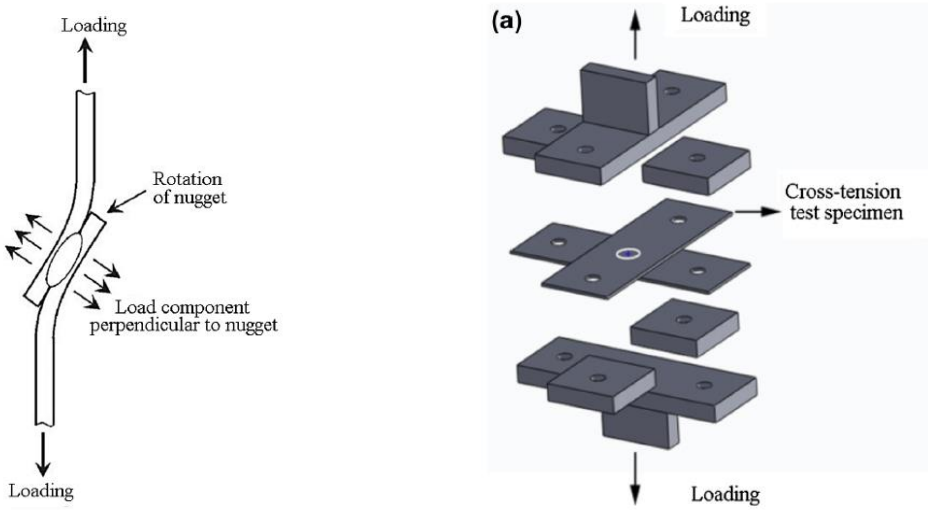

Figure 3.4 - Lap-Shear and Cross-Tensile Loading schemes (Shen *et al,* 2013)

3.5. Metallurgical Characterization

For the metallurgical characterization, the samples were carefully cut using a *Struers Sectotrom-50*. The cut was made 1.5 mm above the centre of the nugget to assure that after the polishing process the centre position was achieved. The samples were polished in a *Struers Tegramin-30* and *Tegrapol-31* in the following steps:

- 320 μm Silicon carbide sandpaper for 30 seconds to 1 minute;
- *Struers Largo* polishing cloth with 9 μm diamond suspension lubricant;
- *Struers Dac* polishing cloth with 3 μm diamond suspension lubricant;
- *Struers Chem* polishing cloth with 1 μm diamond suspension lubricant;
- Electrolytic etching using Barker's Etchant in a *Struers LectroPol-5*.

The evaluation of the microstructural characteristics and defects was made recurring to an optical microscope (OM) *Leica DM IRM* paired with the *Leica Application Suite 3.5* software. The Fracture analysis of the specimens was performed in the scanning electron microscope (SEM) *FEI Quanta 400* by backscattered electron emission.

Finally, the grain size was measured manually using the Interception method in 200x optical microscope images with 6 horizontal lines and 6 vertical lines in each picture.

The measurements were performed according to the ASTM standard for determining grain size (ASTM International, 2004).

3.6. Temperature Measurement

The temperature measurement was performed recurring to two K-type thermocouples that were embedded in the lower sheet, through 0.6 mm holes drilled all the way to the interface. One of the thermocouples was placed in the centre of the weld in order to capture the thermal cycle experienced in the core of the nugget. The other thermocouple was placed 5.5 mm to the outside of the weld, to observe the temperature difference in the Clamping Ring area. The data was collected by a *National Instruments* acquisition system and treated in *LabVIEW* environment. Figure 3.5 illustrates the geometry of the specimen and thermocouple placement.

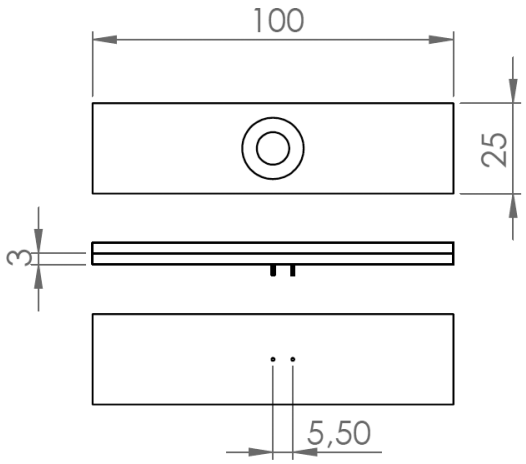

Figure 3.5 – Geometry of the temperature measurement samples and thermocouple placement

4. RESULTS AND DISCUSSION

4.1. Weldability Study

A comprehensive weldability study lead to the conclusion that the values shown on Table 4.1 represent a good starting point for the process development.

Table 4.1 – Initial parameter input

Parameter / Level	*-1*	*0*	*+1*
Rotational Speed [rpm]	2000	2500	3000
Plunge Depth [mm]	2.8	3.3	3.8
Feeding Rate [mm/s]	1.6	2.0	2.4

The maximum rotational speed was chosen according to the maximum advisable speed of the machine, whereas the minimum value was chosen because it represented the minimum rotational speed that could provide a visually sound weld when matched with all the different combinations. The plunge depth window was defined having in consideration previous FSpW studies, in order to comprehend a large range of possibilities, since this parameter's choice of values has very different approaches in different publications. The feeding rate window was built around the value of 2 mm/s, as this rate seemed to produce the best looking welds. Figure 4.1 portrays the typical appearance of a friction spot weld in the material studied in the present work.

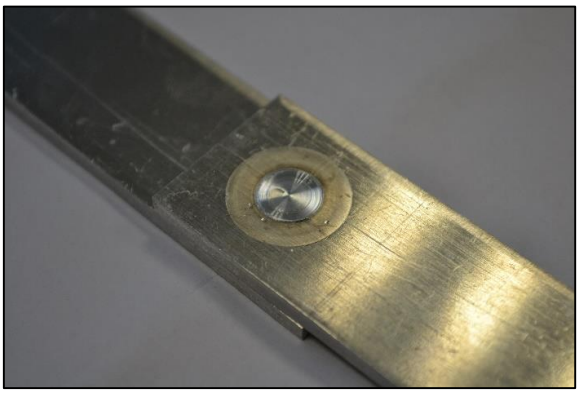

Figure 4.1 – Example of a Friction Spot Weld in AA5454-H22

4.2. Lap-Shear Testing

Prior to the presentation of the process optimization, it is important to refer that a previous study was executed and is presented in Annex B. This study was however discarded due to the changing of components in the machine used for the production of welds, in order to the guarantee the reproducibility of the results.

4.2.1. Box-Behnken DoE

After inputting the selected parameters in the *Minitab* software, the experiments were organized and randomized according to Table 4.2. After Lap-Shear Testing, the results were reported back to *Minitab* software so that an analysis of variance (ANOVA) could be performed and so that the process could be optimized.

The results ranged from about 3.5 kN to 9.6 kN, and from these results alone, it is possible to conclude that the lowest value of plunge depth (2.8 mm) has a notoriously detrimental effect on the LSS of the specimen, since the four lowest results are connected by that common parameter. It is also possible to observe that the centre points of the design (RS=2500; PD=3.3; FR=2) are not the highest ranked specimens in the design, which means that a verification will be necessary to ensure that the best parameter is obtained.

Table 4.2 – Experiment specification and results

Standard Order	*Run Order*	*PtType*	*Blocks*	*RS [rpm]*	*PD [mm]*	*FR [mm/s]*	*PT [s]*	*LSS [N]*
10	1	2	1	2500	3.8	1.6	2.375	9023.21
1	2	2	1	2000	2.8	2.0	1.400	4729.53
8	3	2	1	3000	3.3	2.4	1.375	8438.00
6	4	2	1	3000	3.3	1.6	2.063	9317.02
14	5	0	1	2500	3.3	2.0	1.650	8825.89
7	6	2	1	2000	3.3	2.4	1.375	8935.89
15	7	0	1	2500	3.3	2.0	1.650	8798.3
12	8	2	1	2500	3.8	2.4	1.583	8974.71
9	9	2	1	2500	2.8	1.6	1.750	4717.4
13	10	0	1	2500	3.3	2.0	1.650	9376.97
4	11	2	1	3000	3.8	2.0	1.900	9675.12
11	12	2	1	2500	2.8	2.4	1.167	4691.08
3	13	2	1	2000	3.8	2.0	1.900	8954.38
5	14	2	1	2000	3.3	1.6	2.063	9577.52
2	15	2	1	3000	2.8	2.0	1.400	3510.13

The examination of the analysis of variance of the DoE, on Table 4.3, leads to some conclusions regarding the model and the relation between the parameters and the lap-shear outcome. The confidence level was set at 95%, meaning that p-values under 0.05 will be considered significant (5% error):

- The p-value of the model (0.000) confirms the validity of the model and rejects the null-hypothesis;
- The importance of plunge depth is highlighted by the p-values and contribution values, either in the linear or square approach. The third largest contribution value is the interaction between rotational speed and plunge depth;
- The lack-of-fit value is not relevant according to its p-value and the pure error contribution value is sufficiently small to determine that this parameter window provides a stable model that is valid enough to draw conclusions from.

Table 4.3 – Analysis of variance of the Box-Behnken DoE for LST

Source	*DF*	*Adj. SS*	*Adj. MS*	*Contribution [%]*	*P-Value*
Model	9	65509705	7278856	98.663	0.000
Linear	3	45542346	15180782	68.590	0.000
RS	1	197522	197522	0.297	0.340
PD	1	45026634	45026634	67.814	0.000
FR	1	318191	318191	0.479	0.238
Square	3	19012112	6337371	28.634	0.001
RS · RS	1	4217	4217	0.006	0.884
PD · PD	1	18680713	18680713	28.135	0.000
FR · FR	1	37305	37305	0.056	0.666
2-Way Interaction	3	955247	318416	1.439	0.265
RS ·PD	1	941036	941036	1.417	0.070
RS · FR	1	14089	14089	0.021	0.789
PD · FR	1	123	123	0.000	0.980
Error	5	888019	177604	1.337	-
Lack-of-Fit	3	674916	224972	1.016	0.337
Pure Error	2	213103	106552	0.321	-
Total	14	66397724			

At first sight, the optimization plot seen in Figure 4.2 confirms the prominence of plunge depth in this process for this material, as the variance of this parameter has a much greater effect on the LSS than the changes in rotational speed or feeding rate.

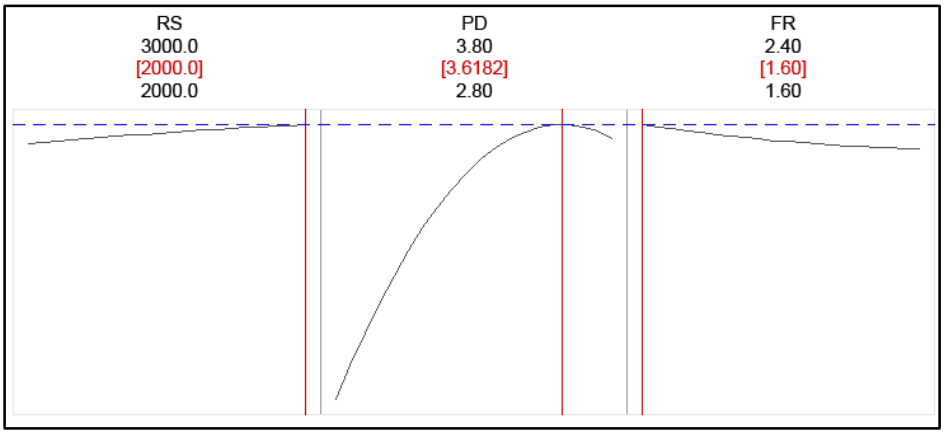

Figure 4.2 – Optimization plot for the chosen parameter range according to *Minitab* software for LSS

According to the analysis of the *Minitab* software, the highest value of rotational speed (3000 rpm) has a positive influence to the lap-shear outcome, although the difference is not large. As 3000 rpm represents the maximum advisable rotational speed for the welding equipment, there is no possibility to try a faster weld and examine the effect of the increase of this parameter.

Regarding plunge depth, there is a maximization point in around 3.6 mm, a value that has not been tried in the first fifteen tests. Although this optimum value is within the chosen range, it becomes necessary to execute new tests to verify the performance of this plunge depth value.

The increase of feeding rate, according to the optimization plot, has a detrimental effect on the strength of the weld. Thus, the optimum value is 1.6 mm/s and it represents the slowest welding speed in the range. However, it is important to test lower feeding rates in order to truly understand if 1.6 mm/s is the best value for this parameter.

In order to test the optimal parameter obtained via Box-Behnken DoE, three trials were made to improve reproducibility and to provide statistical background for the new combination. Table 4.4 portraits the tests and respective results, where is possible to confirm that the best result to date was obtained.

Table 4.4 – Optimum Box-Behnken parameters and results according to *Minitab* software

	Sample Number	*RS* [rpm]	*PD* [mm]	*PR* [mm/s]	*PT* [s]	*LSS* [N]	*Average* [N]	*STDV* [%]
Optimum Box-Behnken	Verification 1	3000	3.6	1.6	2.25	10530.00	10038.59	5.10
	Verification 2					9508.38		
	Verification 3					10077.39		

According to the regression equation provided by the *Minitab* software, as can be seen in Equation (1) and (2), the combination of the optimized parameters should correspond to a 10.055 kN lap-shear strength, that when compared to the average experimental results, 10.038 kN can be considered a very accurate prediction of behaviour. This fact strengthens the validity and stability of this model as a good step in the optimization process.

$$\begin{aligned} \text{LSS}\,(\text{RS}, \text{PD}, \text{FR}) = {} & -86847 - 5.45RS + 59331PD - 2178FR \\ & -8997PD^2 + 628R^2 + 1.940RS \times PD - 0.30RS \times FR - 28PD \times FR \end{aligned} \quad (1)$$

$$\text{LSS}\,(3000, 3.6, 1.6) = 10055.07\ \text{N} \quad (2)$$

4.2.2. One Factor At the Time

The One Factor At the Time approach was employed with two different purposes. The first objective was to verify if 1.6 mm/s was the best choice for the Feeding Rate and to make sure that the maximization point is within the limits of the chosen range and not on its extremities. The second objective is to provide a simpler comparison in terms of microstructure for all the welding conditions. Changing one parameter while maintaining the others is expected to provide a better understanding of the relationship between the parameters and the microstructure of the weld. Each parameter variation in OFAT was named from A to E and compared with the optimum parameter.

Table 4.5 displays the first set of tests where feeding rate was changed between 1.4 mm/s and 1.8 mm/s and the comparison with the optimum parameter. It is therefore possible to conclude that 1.6 mm/s is the optimum value for this parameter as the average lap-shear strength is the highest of the three combinations.

Table 4.5 – OFAT tests for feeding rate

Condition	*Sample Number*	*RS [rpm]*	*PD [mm]*	*FR [mm/s]*	*PT [s]*	*LSS [N]*	*Average [N]*	*STDV [%]*
A	1	3000	3.6	1.4	2.571	9425.55	9837.017	5.02
	2					9701.18		
	3					10384.32		
Optimum (O)	Verification 1	3000	3.6	1.6	2.25	10530.00	10038.59	5.10
	Verification 2					9508.38		
	Verification 3					10077.39		
B	4	3000	3.6	1.8	2.000	9851.44	9689.137	4.49
	5					9196.05		
	6					10019.92		

Although there was already confirmation of the optimum values for plunge depth and rotational speed, additional trials were made and reproduced to be analysed concerning the microstructure. The range was shortened in order to observe more subtle differences in the microstructural properties of each condition.

Table 4.6 depicts the variation of plunge depth and Table 4.7 describes the variation rotational speed. It is possible to observe that the dispersion of the results is considerably smaller than in the Box-Behnken DoE and also it is noticeable that the maximization points occur within the limits of the selected range, confirming once again the validity and stability of the initial model. Figure 4.3 shows a compilation graph of the results so that the effects of each parameter in the LSS can be compared.

Table 4.6 – OFAT tests for plunge depth

Condition	*Sample Number*	*RS [rpm]*	*PD [mm]*	*FR [mm/s]*	*PT [s]*	*LSS [N]*	*Average [N]*	*STDV [%]*
C	BB4	3000	3.3	1.6	2.063	9317.02	9331.28	0.63
	7					9395.68		
	8					9281.13		
Optimum (O)	Verification 1	3000	3.6	1.6	2.25	10530.00	10038.59	5.10
	Verification 2					9508.38		
	Verification 3					10077.39		
D	9	3000	3.9	1.6	2.438	9681.13	10016.28	3.11
	10					10071.49		
	11					10296.21		

Table 4.7 – OFAT tests for rotational speed

Condition	*Sample Number*	*RS [rpm]*	*PD [mm]*	*FR [mm/s]*	*PT [s]*	*LSS [N]*	*Average [N]*	*STDV [%]*
E	12	2700	3.6	1.6	2.250	9961.95	9431.96	9.29
	13					8420.64		
	14					9913.3		
Optimum (O)	Verification 1	3000	3.6	1.6	2.25	10530.00	10038.59	5.10
	Verification 2					9508.38		
	Verification 3					10077.39		

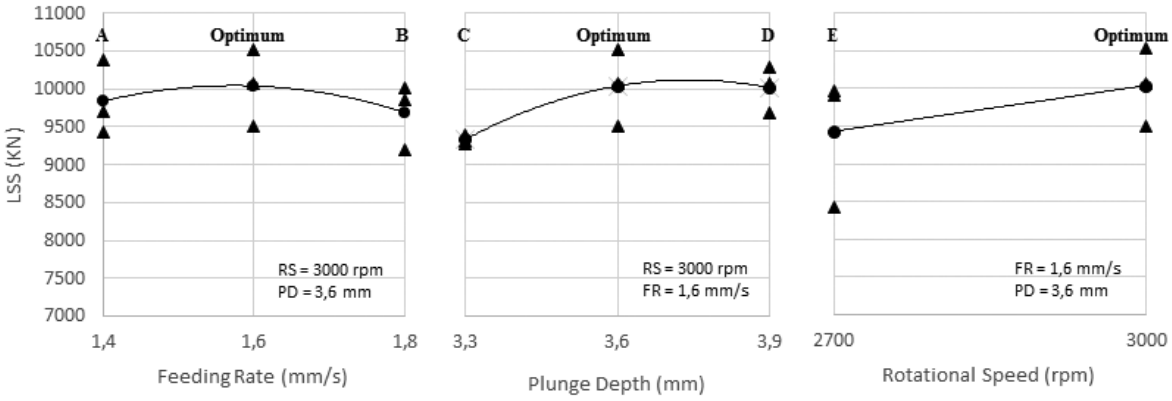

Figure 4.3 – OFAT variation graphs

4.3. Cross-Tensile Testing

Regarding Cross-Tensile Testing, the main objective was to provide complementary information since the amount of material was not large enough to implement a study as comprehensive as the one done for Lap-Shear Testing. For this reason, the same parameter range was used in a Box-Behnken DoE in order to obtain an optimization for both LSS and CTS. The statistical results were once again obtained through the *Minitab* software and although the order of the experiments is not the same on the two DoEs, the results were matched recurring to the standard order.

Table 4.8 displays the experiments and the results each combination lead to. The results exhibit a considerable range, from 0.6 kN to 5.0 kN and despite the fact that the lowest results were obtained with a 2.8 mm PD, it is not possible to make obvious conclusions about the effect of the parameters in the CTS.

Table 4.8 – Cross-Tensile experiments and results

StdOrder	*RunOrder*	*PtType*	*Blocks*	*RS [rpm]*	*PD [mm]*	*FR [mm/s]*	*PT [s]*	*CTS [N]*	*LLS [N]*
3	1	2	1	2000	3.8	2.0	1.900	5032.89	8954.38
15	2	0	1	2500	3.3	2.0	1.650	3648.72	8798.30
13	3	0	1	2500	3.3	2.0	1.650	4260.04	9376.96
11	4	2	1	2500	2.8	2.4	1.167	3174.97	4691.08
7	5	2	1	2000	3.3	2.4	1.375	3541.77	8935.89
5	6	2	1	2000	3.3	1.6	2.063	2731.87	9577.52
14	7	0	1	2500	3.3	2.0	1.650	2337.23	8825.89
6	8	2	1	3000	3.3	1.6	2.063	2821.32	9317.02
9	9	2	1	2500	2.8	1.6	1.750	621.17	4717.40
1	10	2	1	2000	2.8	2.0	1.400	609.49	4729.53
10	11	2	1	2500	3.8	1.6	2.375	2193.85	9023.21
8	12	2	1	3000	3.3	2.4	1.375	2188.33	8438.00
12	13	2	1	2500	3.8	2.4	1.583	2104.88	8974.71
2	14	2	1	3000	2.8	2.0	1.400	975.87	3510.13
4	15	2	1	3000	3.8	2.0	1.900	2226.58	9675.12

Table 4.9 presents the analysis of variance for the DoE, where is possible to observe that contrarily to the results obtained in the LSS, the chosen parameter range is significantly less stable when the samples are tested to CTS.

Table 4.9 – Analysis of variance of the Box-Behnken DoE for CTS

Source	*DF*	*Adj SS*	*Adj MS*	*Contribution [%]*	*P-Value*
Model	9	16242796	1804755	72.696	0.348
Linear	3	7356180	2452060	32.923	0.231
RS	1	1714878	1714878	7.675	0.289
PD	1	4768953	4768953	21.344	0.105
FR	1	872349	872349	3.904	0.436
Square	3	4103585	1367862	18.366	0.424
RS · RS	1	152920	152920	0.684	0.738
PD · PD	1	3696841	3696841	16.546	0.142
FR · FR	1	564480	564480	2.526	0.527
2-Way Interaction	3	4783032	1594344	21.407	0.369
RS ·PD	1	2516490	2516490	11.263	0.21
RS · FR	1	520483	520483	2.329	0.543
PD · FR	1	1746058	1746058	7.815	0.285
Error	5	6100559	1220112	27.304	-
Lack-of-Fit	3	4170254	1390085	18.664	0.435
Pure Error	2	1930305	965153	8.639	-
Total	14	22343356			

An error value of approximately 27% and the lack-of-fit value of almost 19%, combined with the significance value of the model itself, show that it is extremely difficult to draw statistically based conclusions from this trial. However, plunge depth continues to represent the most important contribution in the process whether in linear or square interactions.

Figure 4.4 portrays the optimization plot for the Cross-Tensile Testing. The PD and FR were optimized within the range of experiments, while RS presents a maximization point in the lowest value of the range. When compared to the results obtained in LST, it is possible to observe that plunge depth maximized approximately in the same value while the remaining parameters present opposite behaviours. In the case of CTT, the lowest rotational speed led to the most effective weld, unlike in Lap-Shear Testing. The optimum feeding rate according to the *Minitab* software was also considerably faster than the best parameter found in LST.

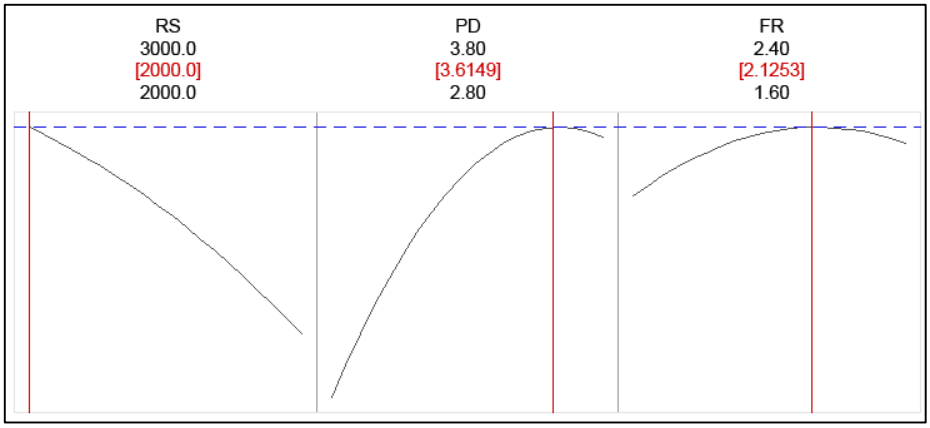

Figure 4.4 – Optimization plot for the chosen parameter range according to *Minitab* software for CTS

Similarly to what was previously done, the optimum parameter was tested in order to verify and validate de model. Table 4.10 shows the experiments and the respective results.

Table 4.10 – Optimum Box-Behnken parameters and results according to *Minitab* software

	Sample Number	*RS* [rpm]	*PD* [mm]	*PR* [mm/s]	*PT* [s]	*LSS* [kN]	*Average* [kN]	*STDV* [%]
Optimum Box-Behnken	Verification 1	2000	3.60	1.60	2.25	3838.38	3877.8767	27.767
	Verification 2					4973.87		
	Verification 3					2821.38		

From this results it is noticeable that the model is not nearly as stable as the one in LST. This conclusion can be confirmed by the values of standard deviation in the same parameter and also by the lack of accuracy in the prediction of the software, shown in Equation (3) and (4).

$$\begin{aligned} \text{LSS (RS, PD, FR)} = {} & -116462 + 17.2RS + 42499PD + 26011FR \\ & -0.00081RS^2 - 4002PD^2 - 2444FR^2 - 3.17RS \times PD \\ & -1.80RS \times FR - 3303PD \times FR \end{aligned} \tag{3}$$

$$\text{LSS } (2000, 3.6, 2.1) = 4311.45 \text{ N} \tag{4}$$

4.4. Fatigue Testing

Fatigue tests were performed in order to better comprehend the behavior of the FSpW welds when submitted to cyclic loads. All welds were produced according to the best parameter obtained in Lap-Shear Testing. Although the standard advises the use of seven test specimens in each level for higher accuracy, due to lack of material, only three samples were tested in each level in other to ensure the maximum reproducibility possible. All samples were tested at 20 Hz until the reference of 5×10^6cycles, where the tests with no fracture were interrupted.

Table 4.11 portrays the five levels of experiments and consequent analysis of the results. Five levels of load were chosen in order to better characterize the fatigue behavior and to find the fatigue limit in this configuration. The Lognormal distribution was used to analyze the probabilistic aspects of the fatigue tests and the Lognormal average of cycles was calculated from the average cycles (μ) and the standard deviation (σ) according to Equation (5).

$$Lognormal\ average\ (N) = e^{\mu + 1.51\sigma^2} \tag{5}$$

It is possible to observe that, when the samples are subjected to 50% of the LSS, the number of cycles is very low and the coefficient of variance (CV) is this highest of all levels. 10% of the LSS, on the other hand, represents the fatigue limit of the material as all samples surpassed the 5 million cycle mark, corresponding to an obvious null value of CV.

Figure 4.5 is the S-N diagram for FSpW in AA5454-H22 and portrays all five levels of fatigue testing and consequent cyclic endurance.

Table 4.11 – Fatigue experiments, results and data analysis

Sample	*LSS Percentage*	$Load_a$	*Cycles*	*Failure*	*Mean (LN(N)), μ*	*Standard deviation, σ*	*Lognormal Mean, Cycles*	*Coefficient of Variance*
F1			4031	Yes				
F2	50%	2258.68	8652	Yes	8.7852	0.4205	8011.91	0.44
F3			8009	Yes				
F10			108423	Yes				
F11	25%	1129.34	89489	Yes	11.6384	0.2617	122674.04	0.27
F12			150185	Yes				
F4			1403196	Yes				
F5	15%	677.6	1688226	Yes	14.2304	0.0967	1530594.10	0.10
F6			1465589	Yes				
F13			2680033	Yes				
F14	12.50%	564.67	4898068	Yes	14.9656	0.3839	3742545.80	0.40
F15			2400616	Yes				
F7			>5000000	No				
F8	10%	451.74	>5000000	No	15.4249	0.0000	5000000.00	0.00
F9			>5000000	No				

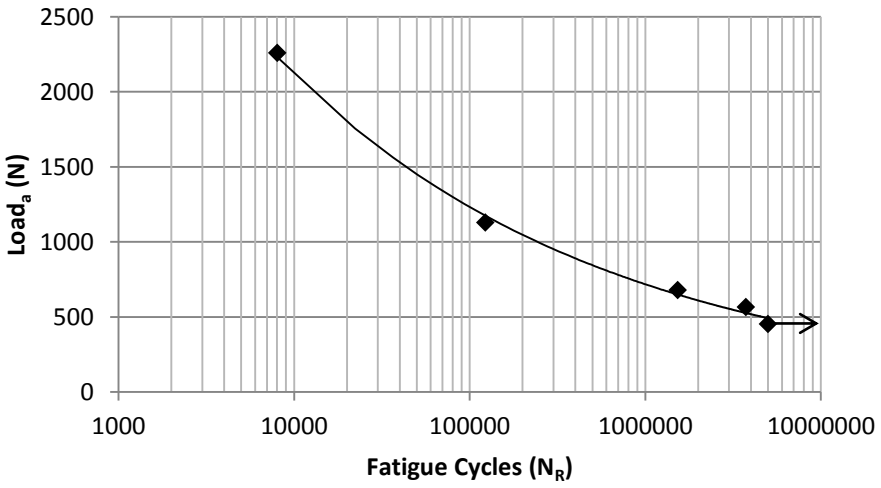

Figure 4.5 – S-N Diagram

A reliability study was also elaborated and is presented in Annex C alongside a graphic representation of the differences of the coefficient of variance in different loading conditions.

4.5. Microstructure

As mentioned during Chapter 4.2, the variations in the parameters were categorized from A to E in order to be compared with the optimum parameter. All the variations were replicated to study the microstructural properties associated with each parameter combination. The macrographs of all the conditions are displayed in Annex D.

Figure 4.6 is the macrograph of the optimum parameter (condition O) where it is possible to observe that the welded area is free of defects such as annular groove or voids. Unlike conditions D and E (Figure D.0.4 and Figure D.0.5), the optimum parameter and conditions A to C (Figure D.0.1 to Figure D.0.3) did not present insufficient refill. A small extrusion of material can be seen on the vicinity of the nugget in all welds due to the gap between the clamping ring and the sleeve.

Figure 4.6 – Macrograph of the cross-section of condition O (FR=1.6; PD=3.6; RS=3000)

The welding nugget presented some similarities in all macrographs:

- The hook defect was found in all conditions, although with different morphologies. Figure 4.7 a) depicts the hook of the optimum weld and a slight bend of the interface in the upper plate. The characteristics of the hook will be thoroughly studied further in this Chapter.
- The bond between plates can only be confirmed in the area affected by the sleeve where there is a clear blend of the materials. The effectiveness of the weld in the centre of the nugget has to be verified recurring to fracture analysis. Figure 4.7 b) displays the plate's interface in the centre of the nugget, where is possible to observe a clear line between the plates.

- Figure 4.7 c) displays the boundary between the area directly affected by the pin and the sleeve and the rest of the plate. On the far right, the base material presents a coarser grain, and with proximity to the nugget, the grain elongates and suffers a slight rotation. The distinction between BM and HAZ cannot be done recurring only to visual inspection. The TMAZ presents highly deformed and elongated grain and the smallest grain can be found in the boundary between the TMAZ and the SZ, coincident with the outer diameter of the sleeve. The SZ is defined by a recrystallized grain, finer than the grain observed in the BM.

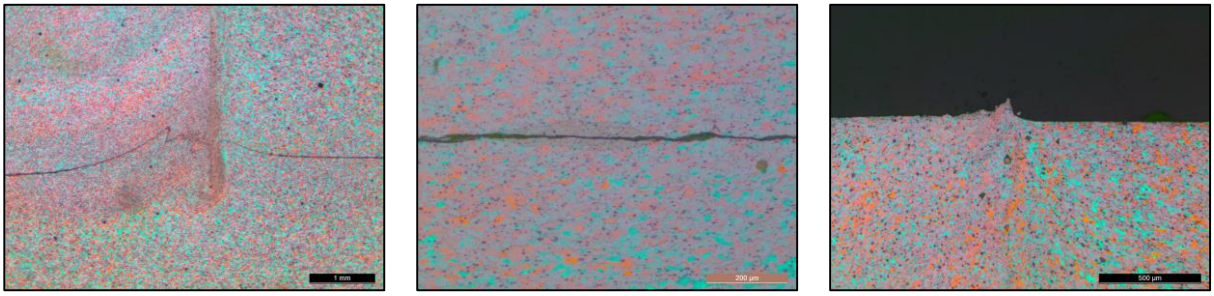

a) Hook defect **b) Bonding ligament** **c) Boundary between SZ and TMAZ**

Figure 4.7 – Microstructural details of condition O

In previous studies it has been stated that some aspects of the hook's morphology and the extension of the nugget correlate directly with the lap-shear strength of the weld. For this reason, various measurements of the hook were made as pictured in Figure 4.8, in order to study the correlations of these characteristics with the strength of the weld.

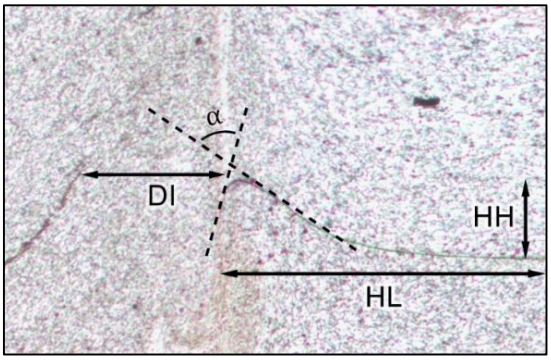

Figure 4.8 – Hook measurement procedure

The hook height (HH) corresponds to the distance from the interface of the plates to the hook tip. The hook length (HL) is the horizontal distance from the hook tip to the point where the interface starts to bend. An approximate hook slope (HS) was also calculated from the aforementioned measurements. The distance between interfaces (DI) represents the distance of the part of the nugget where it is not possible to clearly identify the interface of the plates. The α angle represents the bending angle and aims to quantify the path and the bending of the interface. The bonding area was also measured, corresponding to the distance between the two opposite hook tips. The complete compilation of measurements in presented in Table 4.12.

Table 4.12 – Nugget measurements

Condition	*LSS [kN]*	*Bonding Area [mm]*	*Hook height [mm]*	*Hook Length [mm]*	*Hook slope [°]*	*α [°]*	*Distance between interfaces [mm]*
A	9837.017	9.31	0.20	0.77	14.560	56.38	0.75
B	9689.137	8.84	0.38	1.31	16.176	34.56	0.56
C	9331.277	9.34	0.27	0.98	15.403	84.58	0.46
D	10016.28	8.95	0.46	1.10	22.694	25.34	0.45
E	9431.963	8.98	0.40	1.04	21.038	62.38	0.71
O	10038.59	9.32	0.24	1.09	12.417	21.20	0.45

In order to evaluate the effect of each parameter, the hook analysis was made in two parts. Firstly, the hook morphology was examined regarding individual changes in feeding rate, plunge depth and rotational speed. Secondly, the correlations between each measurement and the lap-shear strength were made in order to try to find common behaviours throughout all conditions.

Figure 4.9 illustrates the changes in the hook's morphology due to the variation of feeding rate. It is possible to conclude that FR has a definite effect on the hook's formation. The most notable differences in these conditions are the α angle between conditions A and O and the HH and HL between conditions O and B. Through the analysis of the pictures and the measurement data is possible to conclude that an increase of FR will contribute to an increase of the HH.

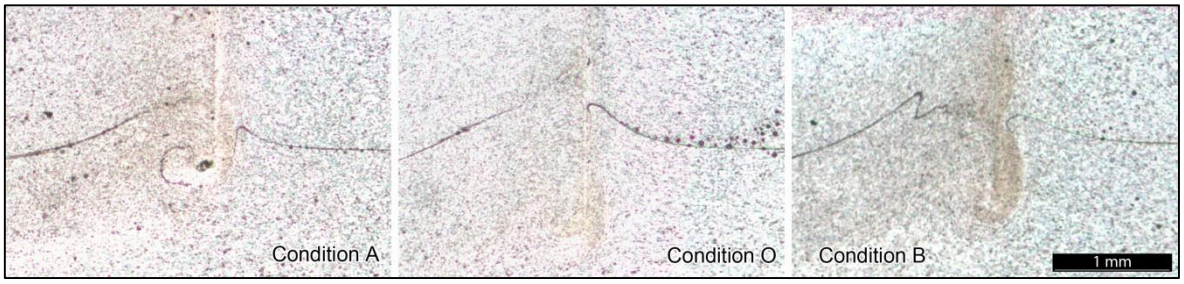

Figure 4.9 – Hook variations in conditions A (FR=1.4; PD=3.6; RS=3000), O (FR=1.6; PD=3.6; RS=3000) and B (FR=1.8; PD=3.6; RS=3000)

Figure 4.10 shows the evolution of hook with the variation of plunge depth. According to Design of Experiments study that was previously made, PD is the parameter with the greatest contribution to the performance of the weld. The hook formation acts accordingly and it is possible to observe that the HH, HS and α angle increase in condition C and D, comparing to condition O.

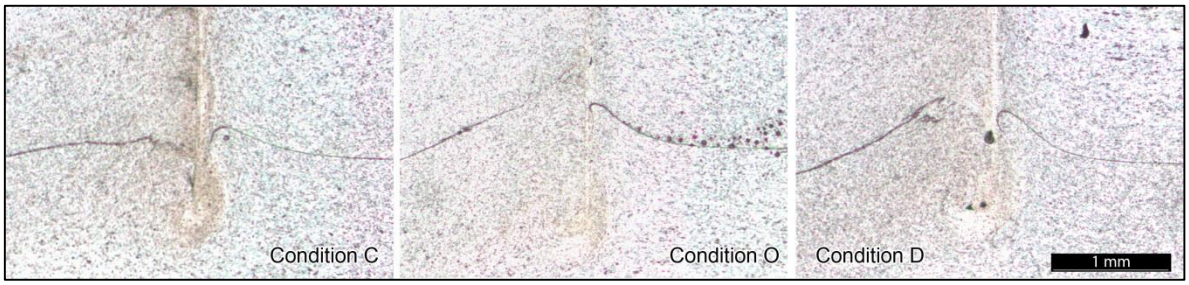

Figure 4.10 – Hook variations in conditions C (FR=1.6; PD=3.3; RS=3000), O (FR=1.6; PD=3.6; RS=3000) and D (FR=1.6; PD=3.9; RS=3000)

Figure 4.11 portrays the hook formation in two different rotational speeds. Similarly to the case of PD, it is noticeable that a low HH and smaller α angles can be associated with higher LSS. Therefore, a decrease in RS will contribute directly to wider α and higher HH.

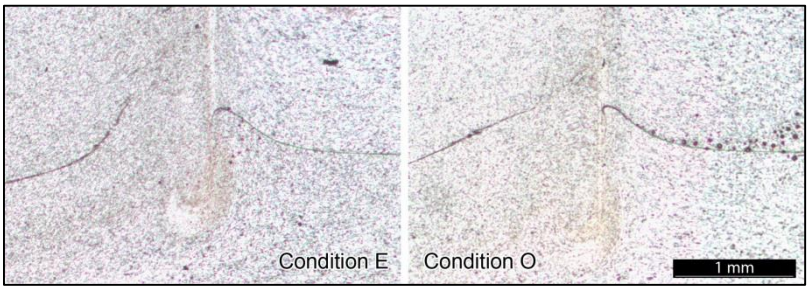

Figure 4.11 – Hook variations in conditions E (FR=1.6; PD=3.6; RS=2700) and O (FR=1.6; PD=3.6; RS=3000)

To evaluate the characteristics of the nugget, regardless of the parameters involved, Pearson's Product-Moment correlation was employed. This method's objective is to establish a linear relationship between two variables. The *r* coefficient varies from -1 to 1 and the larger it is, the stronger the correlation. Equation (6) and Table 4.13 shows, respectively, the formula and criteria for this method.

$$r = \frac{n(\sum xy) - (\sum x)(\sum y)}{\sqrt{[n\sum x^2 - (\sum x)^2]\,[n\sum x^2 - (\sum x)^2]}} \quad (6)$$

Table 4.13 – Correlation strengths for Pearson's Product-Moment correlation

Value of r	*Correlation*
[-1.0; -0.5] or [1.0; 0.5]	Strong
[-0.5; -0.3] or [0.5;0.3]	Moderate
[-0.3;-0.1] to [0.3;0.1]	Weak
[-0.1;0.1]	Very Weak

Table 4.14 presents the Pearson's Product-Moment correlation of each measurement with the LSS.

Table 4.14 – Pearson's Product-Moment correlation

x	*BA [mm]*	*HH [mm]*	*HL [mm]*	*HS [mm]*	*α[°]*	*DI [mm]*
LSS	-0.003	-0.024	0.065	-0.098	-0.885	-0.247

The correlation values are considerably low, except for the α angle. It is worth noticing that the optimum condition has one of the lowest hook heights and hook slope. This suggests that the relation between these factors and the LSS is probably not linear and therefore not detectable by the Pearson´s Product-Moment correlation. However, it is very clear that HH and HS have a definite effect on LSS. The α angle shows a strong relation with the strength of the weld, suggesting that this characteristic dampens or delays the effect of the hook as a crack initiation site. The fact that the tip of the interface is turned backwards can help diverge the critic stress concentration site from the hook tip, which will be the place where the fracture will propagate, regardless of the fracture mode.

4.6. Microhardness & Grain Size

The hardness profiles were studied in order to better evaluate the extension of each affected zone and to try to correlate the microstructural characteristics with the strength of the weld.

The measurements of hardness in the base material in different samples showed a variance between 60 $HV_{0.3}$ and 65 $HV_{0.3}$, granted by the strain-hardening and partial annealing that the material was subjected to. Figure 4.12 pictures the hardness profiles of the optimum condition, as well as the macrograph of the specimen where hardness was measured, in order to facilitate the association of the values with the zone they refer to.

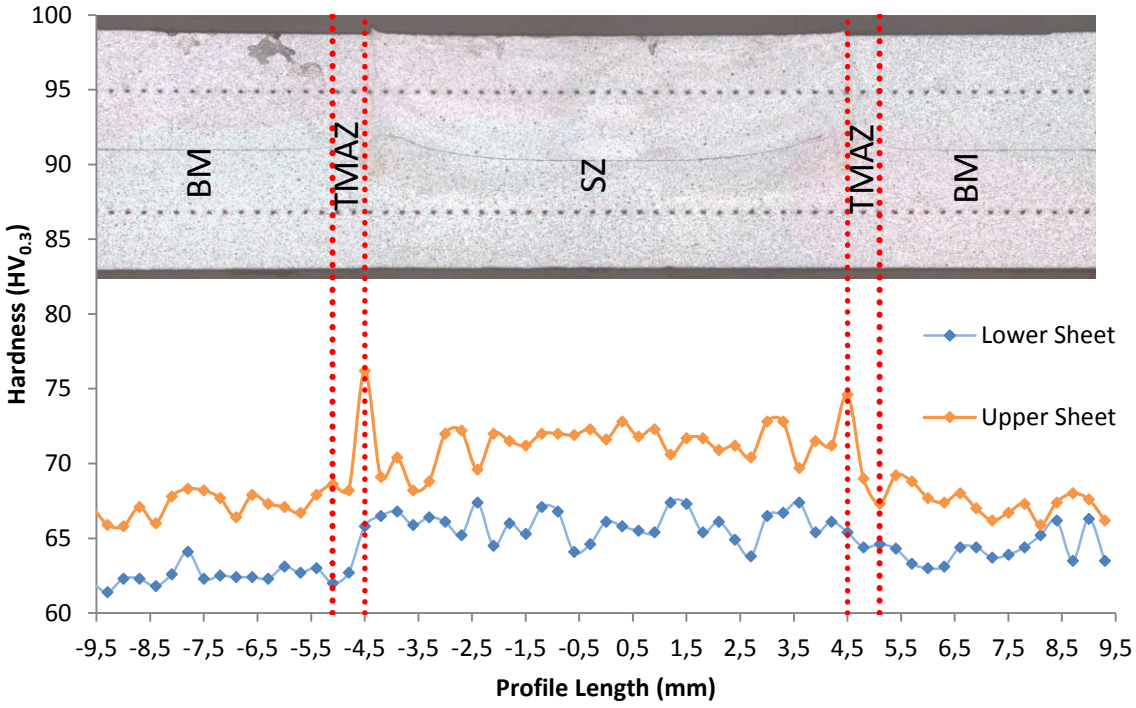

Figure 4.12 – Hardness profiles in the upper and lower plates

In a first general approach, it is interesting to notice that in the total length of the tests there is no loss of hardness compared to the BM. The BM presents relatively steady values in each plate and the SZ presents an increase of around 10% when compared with the original plate. The transition between these two distinct zones shows a drastic upsurge of hardness in each end of the nugget. The two peaks are distanced exactly 9 mm, which matches the outer diameter of the sleeve and corresponds to a zone that was severely stirred.

According to Taha & Hammad (1990) there is a relation between the grain size and hardness in aluminums that can be explained by the Hall-Petch Equation. So, in order to better understand the differences in hardness across the profile, the grain size of various zones was measured in the areas presented in Figure 4.13.

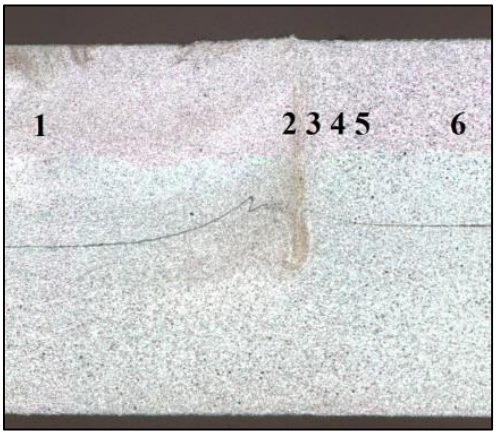

Zone	*Grain Size [µm]*
1	11.11111
2	5.43554
3	15.09434
4	16.00000
5	14.45783
6	13.87283

Figure 4.13 – Grain measurement map and results

The zones were chosen in order to cover all interest points and the detail of each zone is presented in Annex E. Once the grain size values were measured, the data was crossed with the hardness value of the given point with the aim of correlating these two characteristics of the material by the Hall-Petch Relation, shown in Equation (7).

$$H = H_0 + K_H d^{-\frac{1}{2}} \quad (7)$$

According to this equation, the finer the grain, the higher hardness the zone will present. This assumption was verified once the highest hardness values correspond to the lowest grain sizes and vice-versa. In Figure 4.14 it is noticeable that the data has a good fit to this type of equation, showing a satisfying quadratic error value of around 92%.

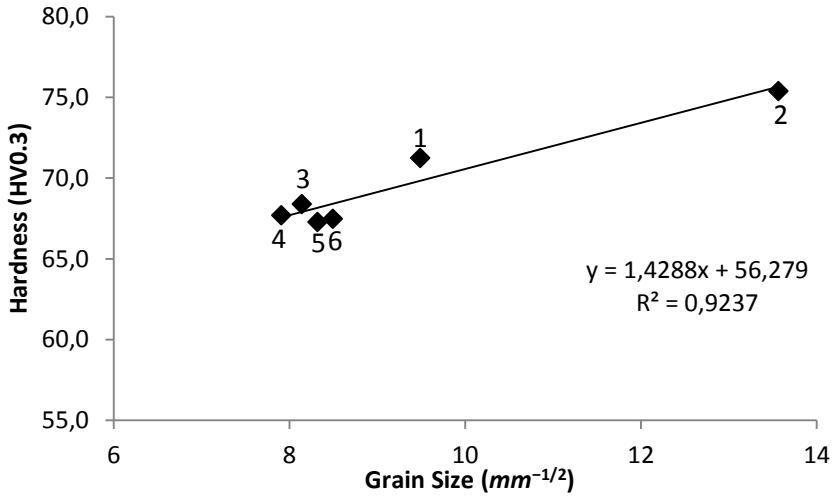

Figure 4.14 – Hall-Petch linear regression graph

Therefore, having in consideration the grain sizes, the weld zones can be defined. The SZ is defined by the outer diameter of the sleeve and the TMAZ is defined by the elongated, coarser grain that extends for 0.6 mm in each side of the nugget. Regarding the rest of the profile, no major differences were found and so the rest of the profile is defined as BM. It is also worth noticing the similitude of the evolution of hardness in the upper and lower plates. The differences can be explained by the reduced plastic deformation of the lower plate.

4.7. Fracture Analysis

During the LST testing procedures, different fracture modes occurred as shown in Figure 4.15. The nomenclature is attributed according to Campanelli *et al* (2013) and a complete table of the fracture modes is presented in Annex F.

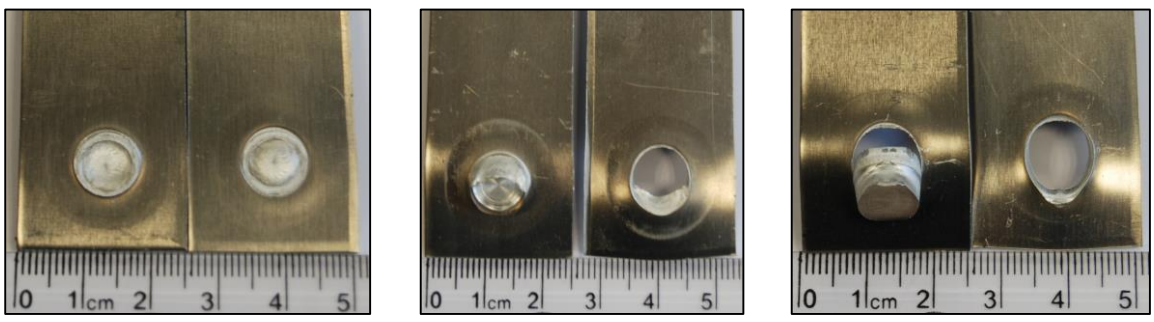

a) Through the Weld **b) Non-Circumferential Pull-out** **c) Circumferential Pull-Out**

Figure 4.15 – Fracture modes observed in Lap-Shear Testing

The most common fracture mode was Through the Weld, illustrated in Figure 4.15 a). This fracture mode is characterized by the propagation of the crack in a direction parallel to the plate's surface, from de hook path to the interface between plates. This fracture mode was verified in the majority of the experiments in condition A to C and O.

Conditions D and E, on the other hand, display an increase of other types of fracture, such as Non-Circumferential Pull-Out, shown in Figure 4.15 b). These two conditions have a high Hook Height in common which leads to a reduction in the cross-section and could facilitate the upward propagation of a crack. This has already been reported by Campanelli *et al* (2013).The Circumferential Pull-Out, seen in Figure 4.15 c) did not happen often enough to draw any conclusions.

The optimum condition for LST fractured in the Through the Weld and Circumferential Pull-Out modes. In the case of CTT, all fractures propagated Through the Weld, as can be observed in Figure 4.16. The SEM fractographic analysis for LST and CTT will be examined further in this Chapter.

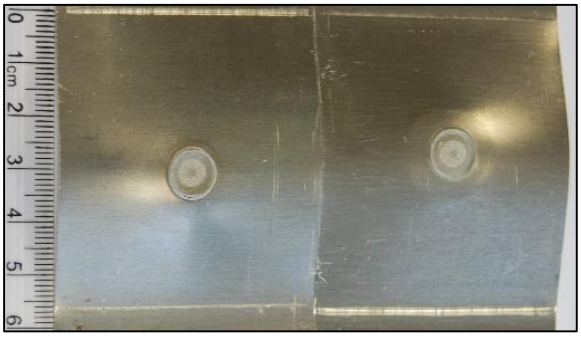

Figure 4.16 – Fracture mode for all CTS specimens

The SEM analysis was carried out with the aim of understanding how the bond between plates changes in the various zones and consequently understand how the different fracture surfaces correlate with mechanical properties. The fractographic images of the several failure modes obtained in LST and CTT are shown in Figures 4.17, 4.18 and 4.19 that will be conveniently presented further in this Chapter.

Figure 4.17 presents the macrograph and some details of the fracture analysis of the Through the Weld mode in LST. Figure 4.17.1 represents the hook area where is possible to observe the boundary between brittle fracture, in the lower part of the image, and ductile fracture, in the upper part. Figure 4.17.2 and Figure 4.17.3, on the other hand, show a considerable density of dimples formed in the direction of the loading, that is generally an

indication of adequate bonding. Figure 4.17.4 displays some typical characteristics of the presence of an oxide layer, like the existence of different fracture planes and the absence of deformation of the material.

Figure 4.18 displays the macrograph and some details of the fracture analysis of the Circumferential Pull-Out mode in LST. In Figure 4.18.1, the surface is clearly fractured in a brittle manner, typical of the hook area, where there is no bonding between the plates. In the other areas there is a significant density of dimples that show the ductile character of this zone.

Due to the fact that it was not possible to make conclusions about the effectiveness of the bonding in the centre of the welds, a SEM analysis of the CTT fracture was performed and is presented in Figure 4.19. It is possible to see a decrease in the ductile character of the fracture and the appearance of surfaces of decohesion between the oxides and the matrix.

The conclusion of this fracture analysis is that it is not possible to guarantee that the bonding in the centre of the nugget is satisfactory, but it is clearly less effective than the bonding in the path of the sleeve. The oxide layer, as it appears only in the centre of the weld, gives the idea that its formation occurs during the process. This phenomena can be caused by the heating of the air trapped on the interface, inside the sleeve, and consequent formation of oxides. The fact that the rotational speed will tend to zero towards the centre of the weld can contribute to a lack of heat input and material deformation in this region that can be insufficient to break the oxide layer. However, to access this possibility, an Energy Dispersive Spectroscopy (EDS) analysis could be done in order to test the presence of oxides in the interface.

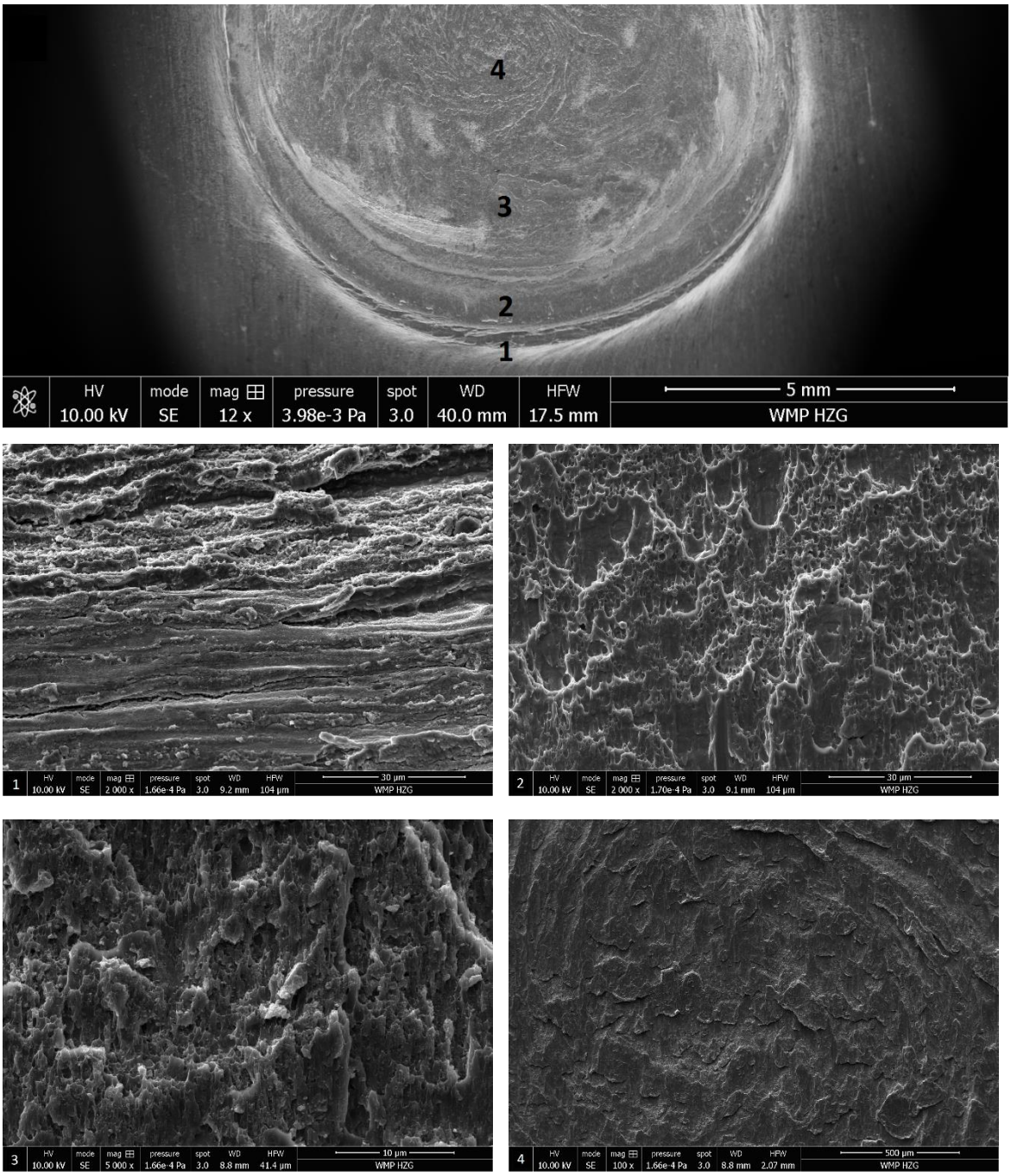

Figure 4.17 – Fractographic Images of the Through the Weld fracture mode in LST (macrograph and details)

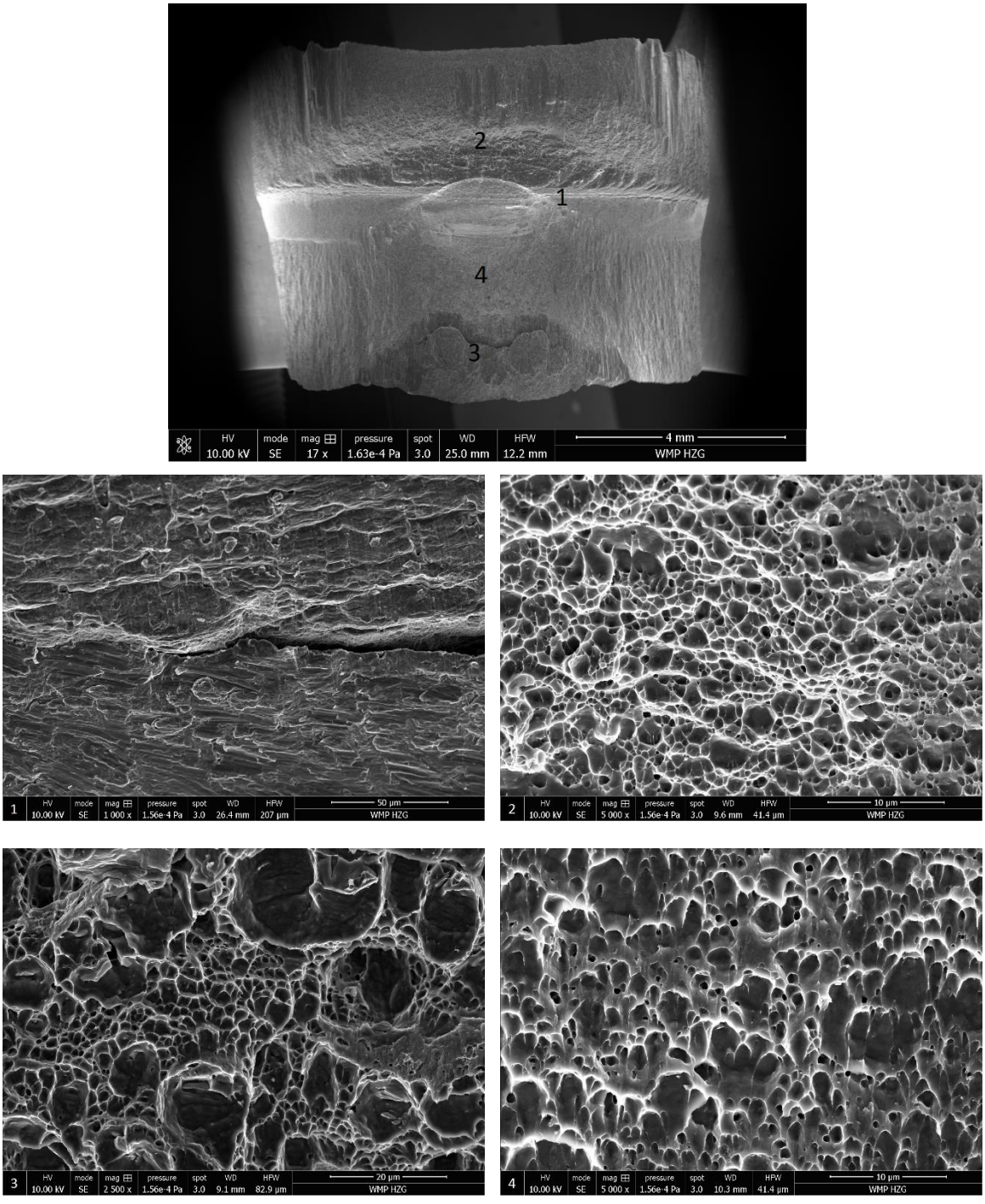

Figure 4.18 – Fractographic Images of the Circumferential Pull-Out fracture mode in LST (macrograph and details)

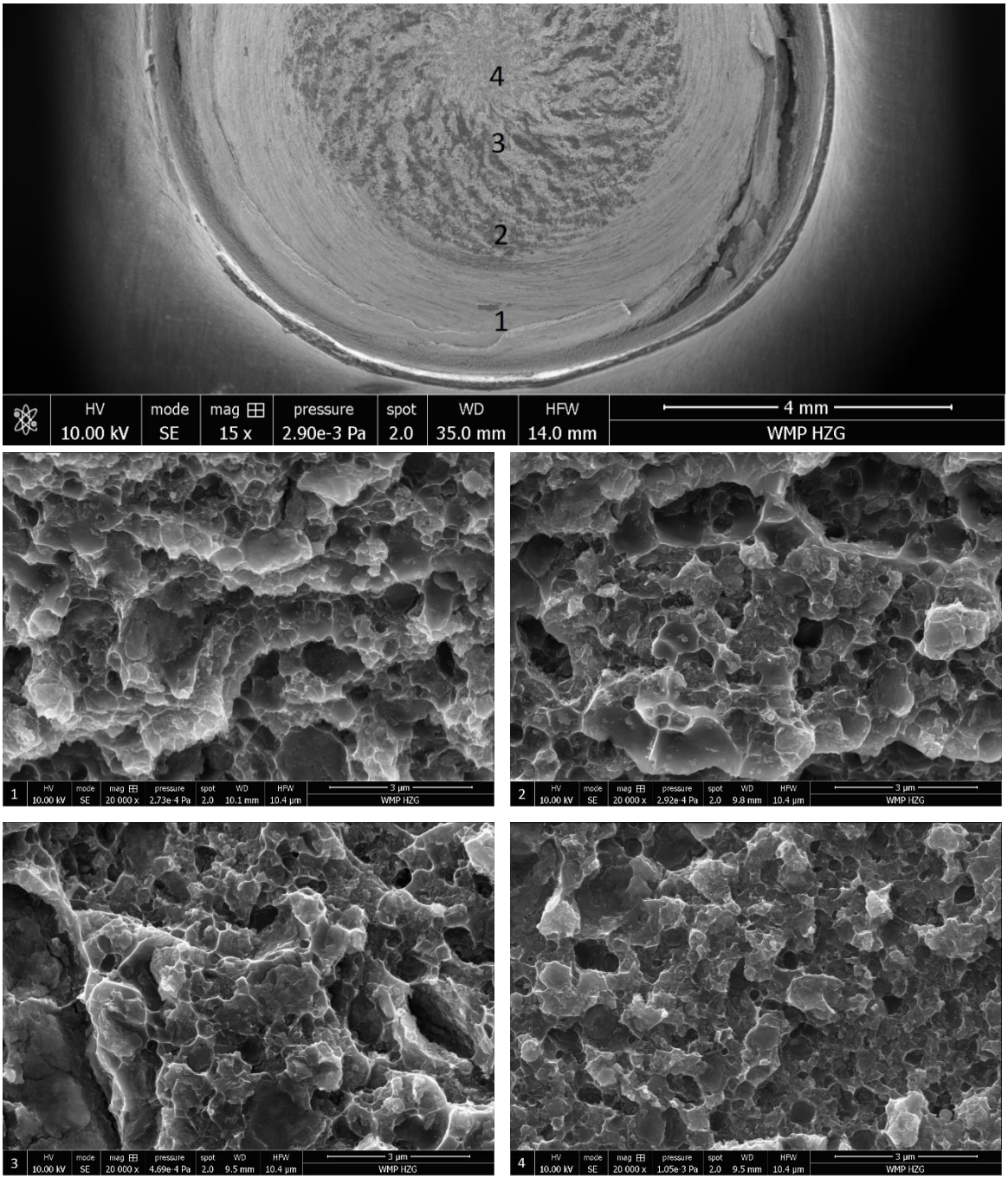

Figure 4.19 – Fractographic Images of the Through the Weld fracture mode in CTT (macrograph and details)

4.8. Temperature Measurement

The process temperatures of the optimum parameter were studied in the area of the pin and the clamping ring with aim to observe the thermal cycle of the different weld zones. Figure 4.20 shows the evolution of the temperature with time in these two areas.

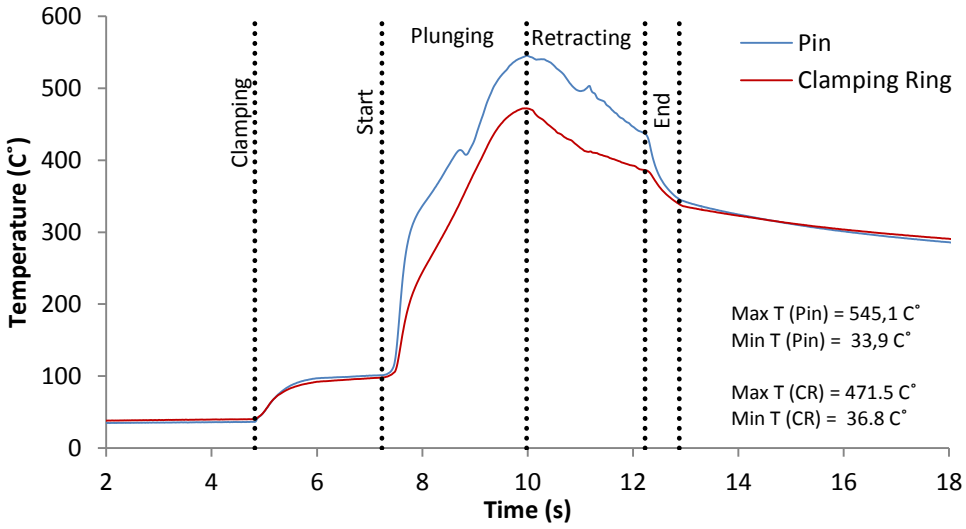

Figure 4.20 – Thermal cycle of the weld

Both thermocouples start at around the same temperature and when the plates are secured by the clamping ring, an increase in temperature to about 100 ˚C can be observed. This upsurge is related to the temperature of the clamping ring, due to the fact that it had been used previously in a short time span. The next step consists of the manual pressing of the start button that initiates the process, after the full approximation of the pin and the sleeve which takes 0.5 seconds.

The welding process itself consists in 2.25 seconds of plunging time and 2.25 seconds of retracting time, as previously stated during the process development. The central thermocouple reaches 545.1 ˚C and the clamping ring's thermocouple reaches the temperature of 471.5 ˚C. After the end of the process, the tools are removed from the surface and the plates are left to cool naturally.

This temperature study confirms that these parameters lead to a high heat input once the highest observed temperatures are considerably close to the melting point of this material which is 607 ˚C.

5. CONCLUSIONS & FUTURE WORK

5.1. Conclusions

First and foremost, it is possible to conclude that the weldability of AA5454-H22 by FSpW is attested. All welds within the parameter range presented a good visual quality and consistent results for Lap-Shear and Fatigue Testing.

The application of a Box-Behnken Design of Experiments was successful in Lap-Shear Testing, as it proved to be a useful tool in finding the optimum parameter, if the parameter range is wide enough. However, this method proved to be difficult and ineffective for the direct analysis of the influence of parameters. To solve this problem, the use of the One Factor At the Time method was fruitful once a good comparison base was built around an optimum parameter. The obtained mark of 10 kN was also satisfying when compared to other works and considering the material.

Regarding the Fatigue Testing, the fatigue limit was obtained at 10% of the LSS, which represents around 1 kN for this specimen's geometry.

The lap shear strength is influenced by the hook geometry; the welds with the narrower α angle lead to a better resistance and a higher hook height influences the fracture mode. The hook height can be associated with a higher heat input but the α angle has no linear relationship with the welding parameters. The lowest value was found for the optimum parameter combination while higher values were found for all other conditions.

The different hardness zones can be explained by the grain size as they are correlated via the Hall-Petch Equation. The grain size was finer in the zones subjected to the greatest deformation such as the vicinity of the stirred zone, where the material was heavily stirred by the sleeve.

5.2. Future Work

In order to improve the current work, there are some further investigations that could be performed such as:

- Additional tests on the cross-tensile configuration to understand the instability of the DoE and try to optimize the parameters to provide a better comparison with Lap-Shear Testing;
- Elaboration of a more comprehensive test on fatigue, with more levels and more samples per level;
- Further analysis of the microstructure with more conditions and a wider variation of parameters;
- Application of the α angle to other FSpW studies to confirm the applicability of this parameter to other materials and configurations;
- EDS analysis to the bonding ligament to verify the presence of oxides;
- Analysis of fracture to fatigue samples in order to understand the propagation of the cracks under cyclic loading;
- Testing the same parameters with a thicker sleeve and narrowed pin. The bonding was more effective in the sleeve's path and it would be interesting to increase the area directly affected by the sleeve to understand the influence this could have on the microstructure and fracture surface.

BIBLIOGRAPHY

ALCOA Inc., 2015. ALCOA. Available at: http://www.alcoa.com/.

Amancio-Filho, S.T. et al., 2011. Preliminary Investigation of the Microstructure and Mechanical Behaviour of 2024 Aluminium Alloy Friction Spot Welds. *Materials Transactions*, 52(5), pp.985–991. Available at: http://joi.jlc.jst.go.jp/JST.JSTAGE/matertrans/L-MZ201126?from=CrossRef.

ASM International, 2008. Fatigue, Chapter 14.

ASTM International, 2004. ASTM E 112-96(2004) Standard Test Methods for Determining Average Grain Size. , p.26. Available at: http://image.sciencenet.cn/olddata/kexue.com.cn/bbs/upload/9943ASTM_standard__E_112_standard_test_methods_for_determining_average_grain_size.pdf.

AZOMaterials, 2015. AZO Materials. Available at: http://www.azom.com/.

Badarinarayan, H. et al., 2009. Effect of tool geometry on hook formation and static strength of friction stir spot welded aluminium 5754-O sheets. *Int J Mach Tools Manuf*, 49(814-23).

Branco, C.A.G. de M. et al., 2012. *Projecto de Orgãos de Máquinas*, Fundação Calouste Gulbenkian.

Çam, G. & Mistikoglu, S., 2014. Recent developments in friction stir welding of al-Alloys. *Journal of Materials Engineering and Performance*, 23(6), pp.1936–1953.

Campanelli, L.C. et al., 2013. Metallurgy and mechanical performance of AZ31 magnesium alloy friction spot welds. *Journal of Materials Processing Technology*, 213(4), pp.515–521. Available at: http://dx.doi.org/10.1016/j.jmatprotec.2012.11.002.

Cobden, R., Alcan & Banbury, 1994. *Aluminium: Physical Properties, Characteristics and Alloys*,

Engler, O., Liu, Z. & Kuhnke, K., 2013. Impact of homogenization on particles in the Al–Mg–Mn alloy AA 5454 – Experiment and simulation. *Journal of Alloys and Compounds*, 560, pp.111–122. Available at: http://www.sciencedirect.com/science/article/pii/S0925838813002260.

Etter, a. L. et al., 2007. Recrystallization mechanisms in 5251 H14 and 5251 O aluminum friction stir welds. *Materials Science and Engineering: A*, 445-446, pp.94–99. Available at: http://linkinghub.elsevier.com/retrieve/pii/S0921509306020028.

ISO International, 2000. International Standard 14272 - Specimen dimensions and

procedure for cross tension testing resistance spot and embossed projection welds.

ISO International, 2014. International Standard 14273.2 - Resistance Welding - Destructive testing of welds - Specimendimensions and procedure for tensile shear testing resistance spot, seam and embossed projection welds.

ISO International, 2003. International Standard 14324 - Resistance Spot Welding - Destructive tests of welds - Method for the fatigue testinf of spot welded joints.

MATTER & Liverpool, U., 2010. AluMatter. Available at: http://aluminium.matter.org.uk/.

Mishra, R.S. & Ma, Z.Y., 2005. Friction stir welding and processing. *Materials Science and Engineering R: Reports*, 50(1-2), pp.1–78.

Online, M.S., 2015. Suppliers Online. Available at: http://www.suppliersonline.com/.

Rosendo, T. et al., 2011. Mechanical and microstructural investigation of friction spot welded AA6181-T4 aluminium alloy. *Materials and Design*, 32(3), pp.1094–1100. Available at: http://dx.doi.org/10.1016/j.matdes.2010.11.017.

RUSAL, U., 2015. Aluminium Leader. Available at: http://www.aluminiumleader.com/.

Shen, Z. et al., 2013. Microstructure and failure mechanisms of refill friction stir spot welded 7075-T6 aluminum alloy joints. *Materials and Design*, 44, pp.476–486. Available at: http://dx.doi.org/10.1016/j.matdes.2012.08.026.

Shen, Z. et al., 2014. Microstructure and mechanical properties of friction spot welded 6061-T4 aluminum alloy. *Materials & Design*, 54, pp.766–778. Available at: http://linkinghub.elsevier.com/retrieve/pii/S0261306913007656.

Suhuddin, U. et al., 2014. Microstructure and mechanical properties of friction spot welds of dissimilar AA5754 Al and AZ31 Mg alloys. *Materials Science and Engineering A*, 590, pp.384–389. Available at: http://dx.doi.org/10.1016/j.msea.2013.10.057.

Suhuddin, U.F.H., Fischer, V. & Dos Santos, J.F., 2013. The thermal cycle during the dissimilar friction spot welding of aluminum and magnesium alloy. *Scripta Materialia*, 68(1), pp.87–90. Available at: http://dx.doi.org/10.1016/j.scriptamat.2012.09.008.

Taha, A.S. & Hammad, F.H., 1990. Application of the {Hall-Petch} Relation to Microhardness Measurements on Al, Cu, {Al-MD} 105, and {Al-Cu} Alloys. *Phys. Status Solidi*, 119(2), pp.455–462.

Threadgill, P.L., 2010. *The future of friction stir welding*, Woodhead Publishing Limited. Available at: http://linkinghub.elsevier.com/retrieve/pii/B9781845694500500064.

Tier, M.D. et al., 2013. The influence of refill FSSW parameters on the microstructure and shear strength of 5042 aluminium welds. *Journal of Materials Processing Technology*, 213(6), pp.997–1005. Available at: http://dx.doi.org/10.1016/j.jmatprotec.2012.12.009.

Venâncio, M., 2013. *Friction Spot Welding Da Liga De Alumínio 6082-T6*. Universidade de Coimbra.

Yang, X.W., Fu, T. & Li, W.Y., 2014. Friction stir spot welding: A review on joint macro- and microstructure, property, and process modelling. *Advances in Materials Science and Engineering*, 2014.

Zhao, Y.Q. et al., 2014. Effects of sleeve plunge depth on microstructures and mechanical properties of friction spot welded alclad 7B04-T74 aluminum alloy. *Materials and Design*, 62, pp.40–46. Available at: http://dx.doi.org/10.1016/j.matdes.2014.05.012.

ANNEX A

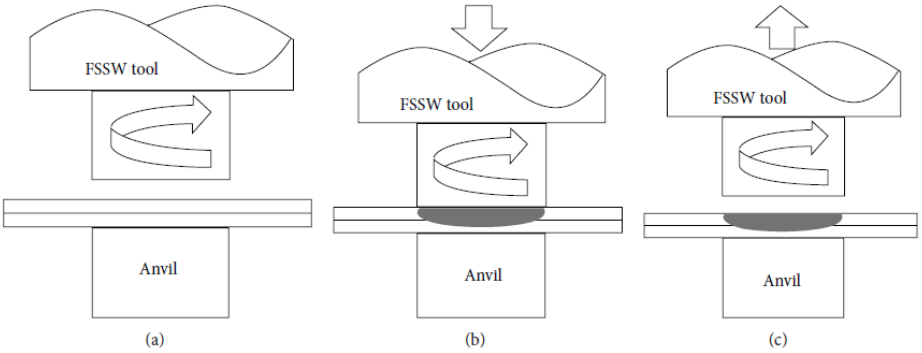

Figure A.0.1 - Pinless FSSW process

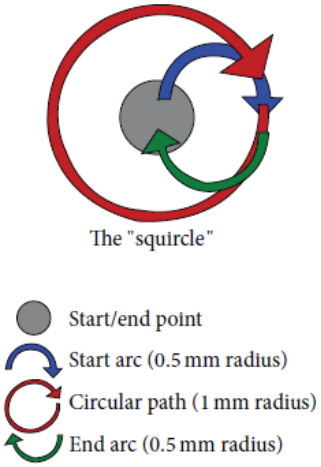

Figure A.0.2 - Swing FSSW process

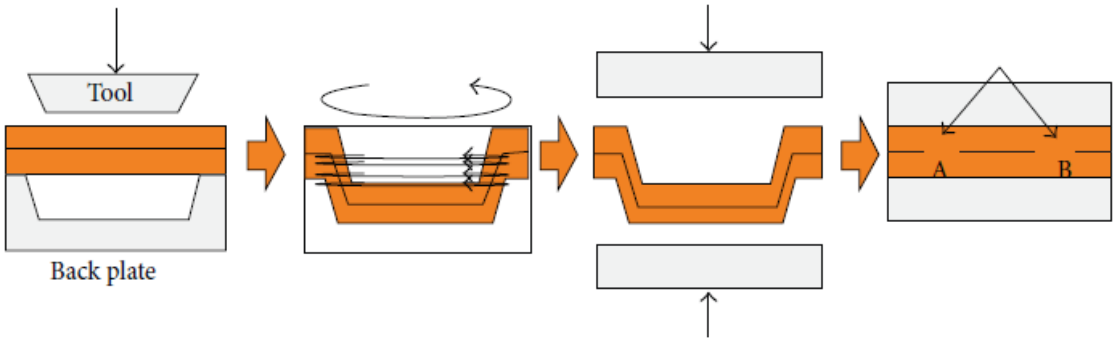

Figure A.0.3 - Novel FSSW process

ANNEX B

Table B.0.1 – Experiments and results for the first Box-Behnken DoE

StdOrder	*RunOrder*	*PtType*	*Blocks*	*RS [rpm]*	*PD [mm]*	*FR [mm/s]*	*PT [s]*	*LSS [kN]*
10	1	2	1	1750	3.2	2.2	1.455	8979.72
15	2	0	1	1750	3.0	2.4	1.250	6786.74
4	3	2	1	2000	3.2	2.4	1.333	8542.37
12	4	2	1	1750	3.2	2.6	1.231	8484.54
8	5	2	1	2000	3.0	2.6	1.154	7090.37
14	6	0	1	1750	3.0	2.4	1.250	7099.46
7	7	2	1	1500	3.0	2.6	1.154	6352.89
13	8	0	1	1750	3.0	2.4	1.250	6375.03
11	9	2	1	1750	2.8	2.6	1.077	5843.9
9	10	2	1	1750	2.8	2.2	1.273	5623.49
2	11	2	1	2000	2.8	2.4	1.167	5107.57
1	12	2	1	1500	2.8	2.4	1.167	5786.54
3	13	2	1	1500	3.2	2.4	1.333	8521.49
5	14	2	1	1500	3.0	2.2	1.364	6888.66
6	15	2	1	2000	3.0	2.2	1.364	7679.74

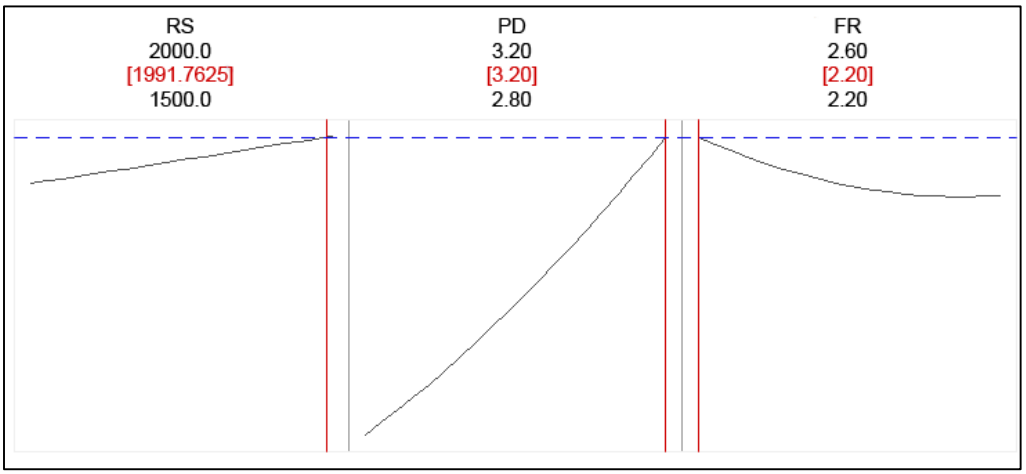

Figure B.0.1 – Optimization plot for the first Box-Behnken DoE

Table B.0.2 – Analysis of variance for the first Box-Behken DoE

Source	*DF*	*Adj. SS*	*Adj. MS*	*Contribution [%]*	*P-Value*
Model	9	19491831	2165759	95.33	0.008
Linear	3	18843014	6281005	92.15	0.001
RS	1	94715	94715	0.46	0.513
PD	1	18503330	18503330	90.49	0
FR	1	244969	244969	1.20	0.309
Square	3	397635	132545	1.94	0.594
RS · RS	1	31	31	0.02	0.99
PD · PD	1	200234	200234	0.83	0.353
FR · FR	1	223981	223981	1.10	0.328
2-Way Interaction	3	251183	83728	1.23	0.736
RS · PD	1	122448	122448	0.60	0.46
RS · FR	1	718	718	0.00	0.953
PD · FR	1	128017	128017	0.63	0.45
Error	5	955839	191168	4.67	-
Lack-of-Fit	3	691807	230602	3.38	0.384
Pure Error	2	264033	132016	1.29	-
Total	14	20447671			

Table B.0.3 – Experiments and results of the second Box-Behnken DoE

StdOrder	*RunOrder*	*PtType*	*Blocks*	*RS [rpm]*	*PD [mm]*	*FR [mm/s]*	*PT [s]*	*LSS [kN]*
15	1	0	1	2000	3.4	2.0	1.700	8145.1
10	2	2	1	2000	3.6	1.8	2.000	7971.26
6	3	2	1	2250	3.4	1.8	1.889	8798.24
2	4	2	1	2250	3.2	2.0	1.600	9456.85
13	5	0	1	2000	3.4	2.0	1.700	7996.37
14	6	0	1	2000	3.4	2.0	1.700	7764.7
11	7	2	1	2000	3.2	2.2	1.455	8863.99
3	8	2	1	1750	3.6	2.0	1.800	8249.43
7	9	2	1	1750	3.4	2.2	1.545	6875.7
8	10	2	1	2250	3.4	2.2	1.545	7309.22
1	11	2	1	1750	3.2	2.0	1.600	9008.4
9	12	2	1	2000	3.2	1.8	1.778	8782.94
12	13	2	1	2000	3.6	2.2	1.636	7316.83
5	14	2	1	1750	3.4	1.8	1.889	8345.27
4	15	2	1	2250	3.6	2.0	1.800	7789.59

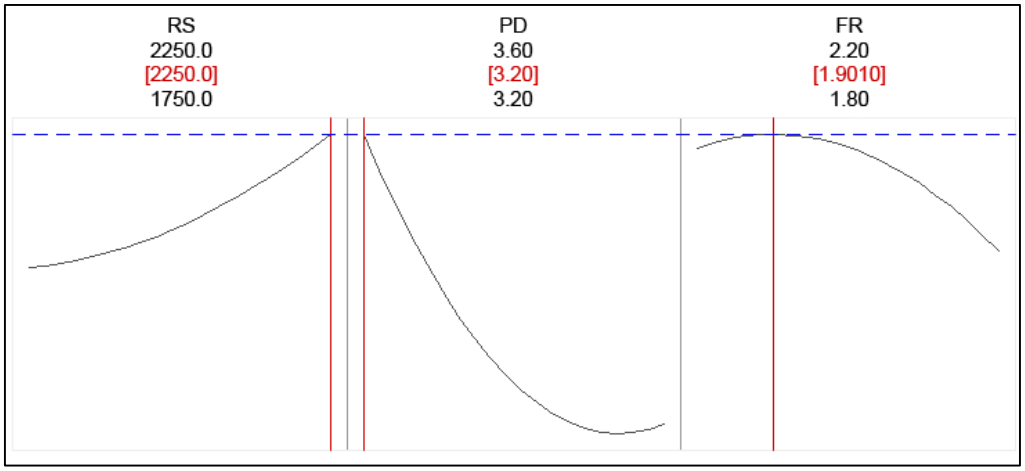

Figure B.0.2 – Optimization plot for the second Box-Behken DoE

Table B.0.4 – Analysis of variance of the second Box-Behnken DoE

Source	*DF*	*Adj SS*	*Adj MS*	*Contribution [%]*	*P-Value*
Model	9	6284211	698246	87.64	0.073
Linear	3	4517188	1505729	63.00	0.021
RS	1	95725	95725	1.34	0.495
PD	1	2862112	2862112	39.92	0.01
FR	1	1559352	1559352	21.75	0.031
Square	3	1425448	475149	19.88	0.158
RS · RS	1	60351	60351	0.62	0.585
PD · PD	1	1035197	1035197	15.66	0.06
FR · FR	1	258245	258245	3.60	0.281
2-Way Interaction	3	341575	113858	4.76	0.62
RS ·PD	1	206248	206248	2.88	0.33
RS · FR	1	95	95	0.00	0.982
PD · FR	1	135233	135233	1.89	0.422
Error	5	885993	177199	12.36	-
Lack-of-Fit	3	812495	270832	11.33	0.122
Pure Error	2	73499	36749	1.03	-
Total	14	7170205			

ANNEX C

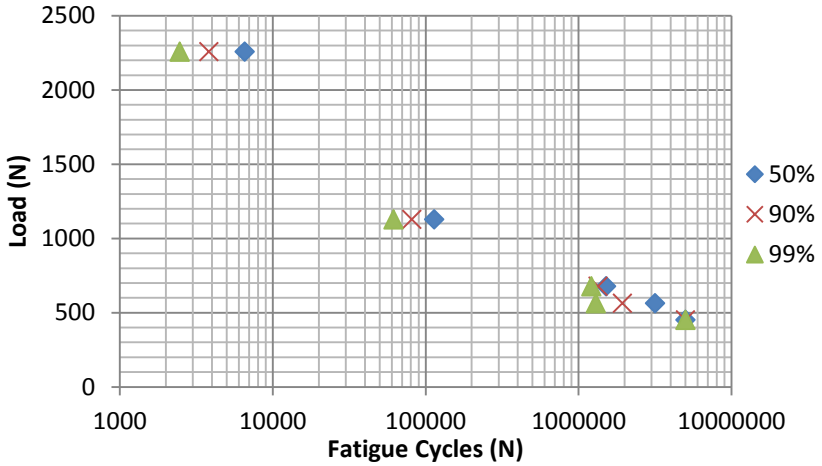

Figure C.0.1 – Reliability S-N Diagram

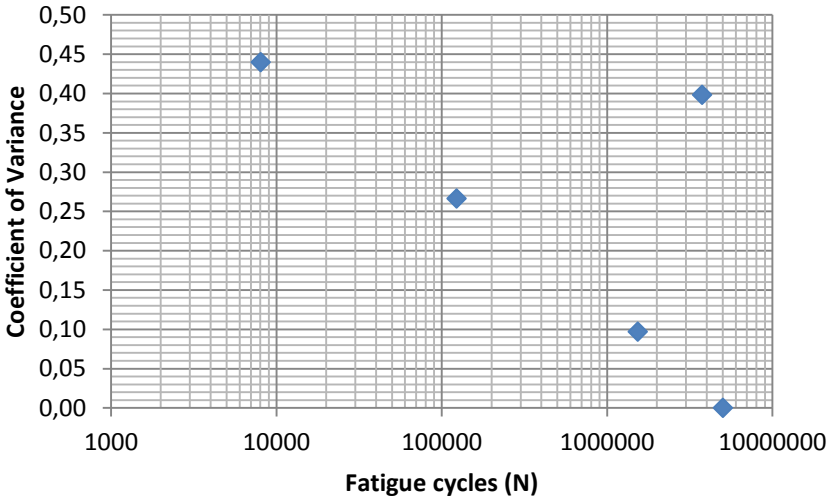

Figure C.0.2 – Coefficients of variance

ANNEX D

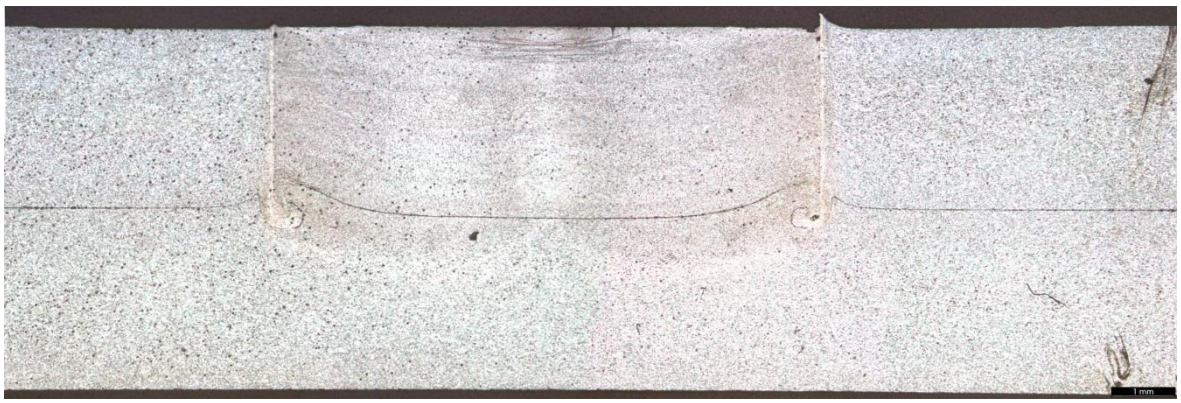

Figure D.0.1 – Macrograph of condition A

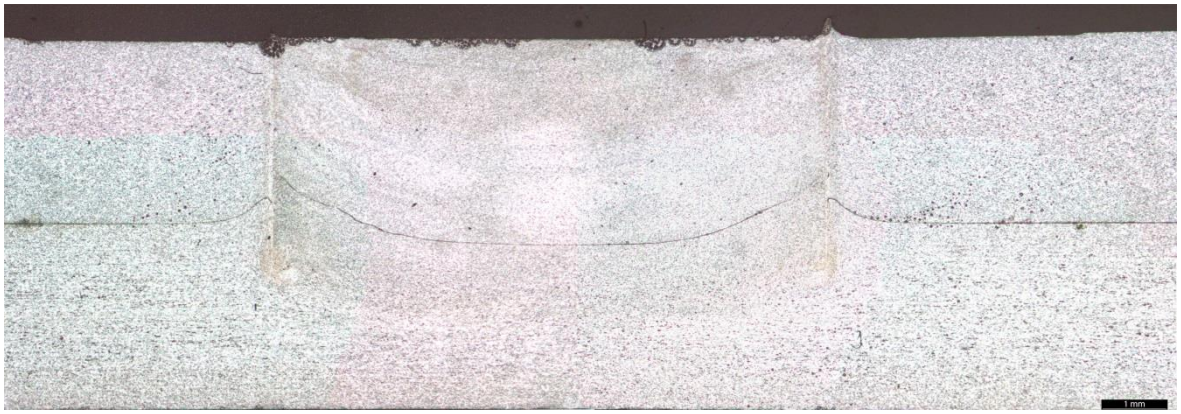

Figure D.0.2 – Macrograph of condition B

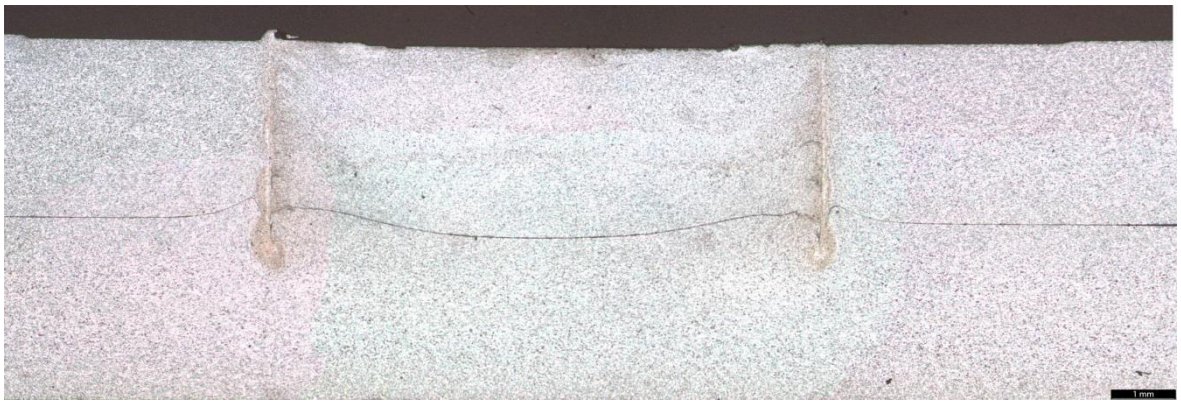

Figure D.0.3 – Macrograph of condition C

Figure D.0.4 – Macrograph of condition D

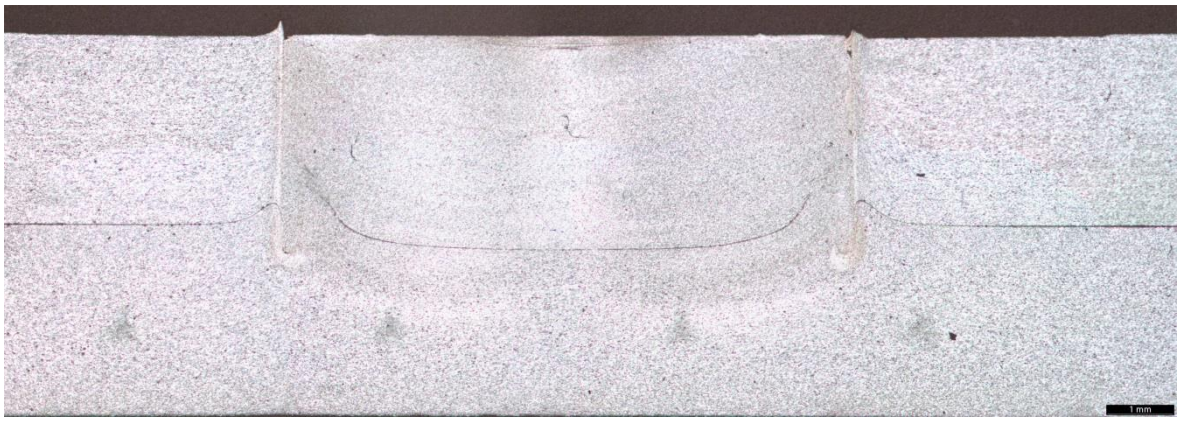

Figure D.0.5 – Macrograph of condition E

Figure D.0.6 – Macrograph of condition O

ANNEX E

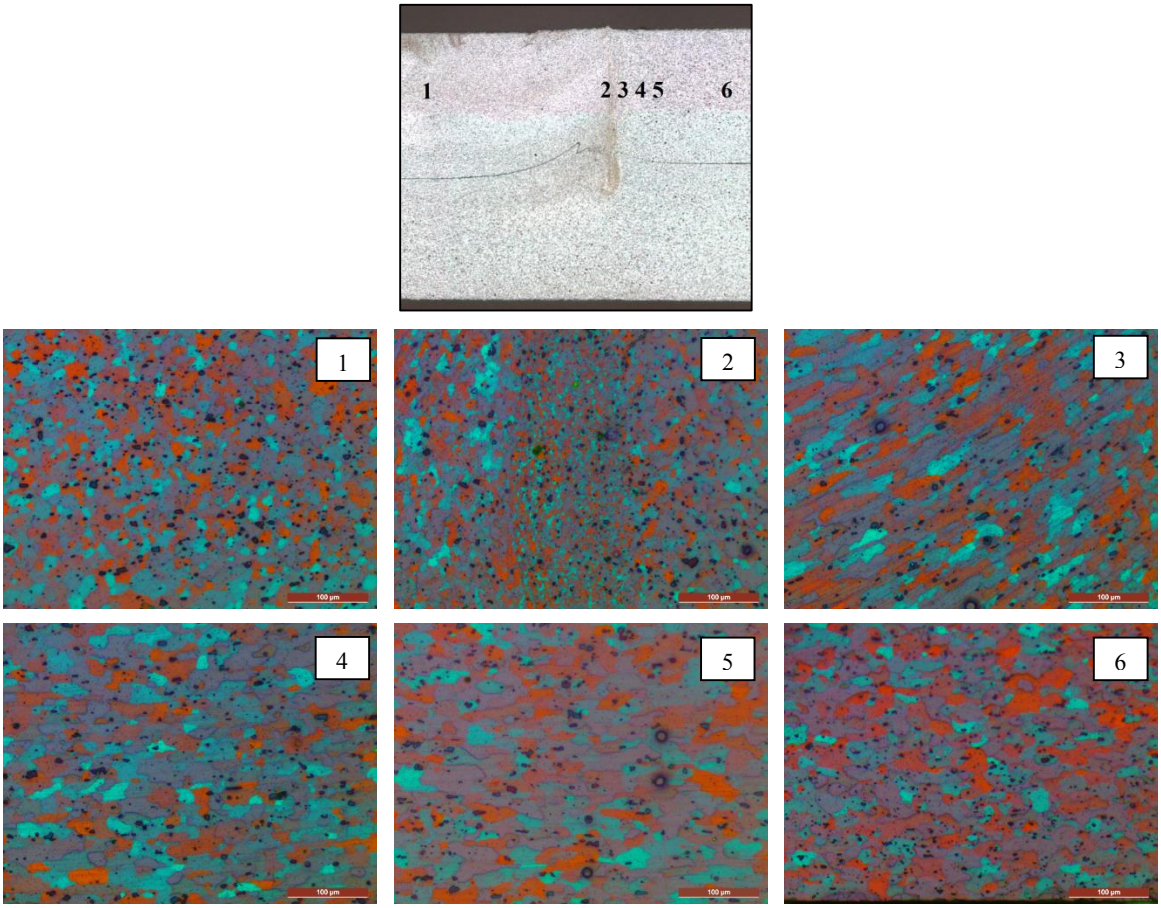

Figure E.0.1 – Detail of the weld zones where the grain size was measured

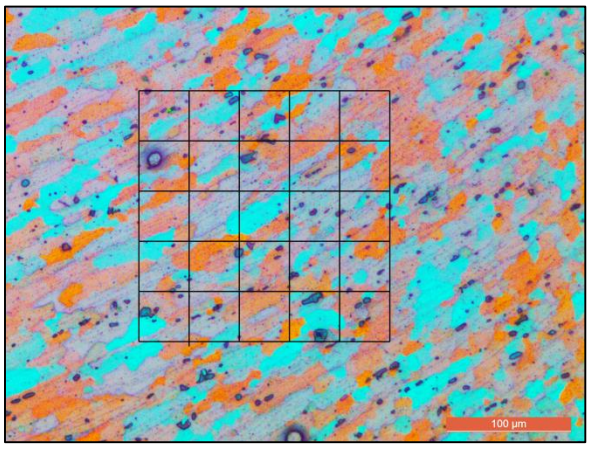

Figure E.0.2 – Grain Size measurement procedure example, zone 3

ANNEX F

Table F.0.1 – Fracture modes for OFAT experiments

Conditions	*LSS [kN]*	*Av. LSS [kN]*	*Fracture Mode*
	9425 .55		Circumferential Pull-out
A	9701 .18	9837 .017	Through the Weld
	10384 .32		Through the Weld
	9851 .44		Through the Weld
B	9196 .05	9689 .137	Through the Weld
	10019 .92		Through the Weld
	9317 .02		Through the Weld
C	9395 .68	9331 .277	Through the Weld
	9281 .13		Through the Weld
	9681 .13		Non-Circumferential Pull-Out
D	10071 .49	10016 .28	Non-circumferential Pull-Out
	10296 .21		Through the Weld
	9961 .95		Non-Circumferential Pull-Out
E	8420 .64	9431 .963	Through the Weld
	9913 .30		Through the Weld
	10530.00		Through the Weld
O	9508 .38	10038 .59	Through the Weld
	10077 .39		Circumferential Pull Out